

# An Efficient Algorithm for the Multicomponent Compressible Navier-Stokes Equations in Low and High Mach Number Regimes.

Roman Frolov<sup>1</sup>

<sup>a</sup>*Department of Mathematical and Statistical Sciences, University of Alberta, Edmonton, AB, Canada*

---

## Abstract

The goal of this study is to develop an efficient numerical algorithm applicable to a wide range of compressible multicomponent flows, including nearly incompressible low Mach number flows, flows with strong shocks, multicomponent flows with high density ratios and interfacial physics, inviscid and viscous flows, as well as flows featuring combinations of these phenomena and various interactions between them. Although many highly efficient algorithms have been proposed for simulating each type of the flows mentioned above, a construction of universal solvers is known to be challenging. Extreme cases, such as incompressible and highly compressible flows, or inviscid and viscous flows, require different numerical treatments in order to maintain efficiency, stability, and accuracy of the method.

Linearized block implicit (LBI) factored schemes (see e.g. [1], [2]) are known to provide an efficient way of solving the compressible Navier-Stokes equations implicitly, which allows avoiding stability restrictions at low Mach number and high viscosity. However, their splitting error has been shown to grow as the Mach number goes to zero and dominate physical fluxes (see [3]). In this paper, a splitting error reduction technique is proposed to solve the issue. A shock-capturing algorithm from [4] is reformulated in terms of finite differences, extended to the stiffened gas equation of state (SG EOS) and combined with the LBI factored scheme to stabilize the method around flow discontinuities at high Mach numbers. A novel stabilization term is proposed for low Mach number applications. The resulting algorithm is shown to be efficient in both low and high Mach number regimes. The algorithm is further extended to the multicomponent case using an interface capturing strategy (see e.g. [5]) with surface tension as a continuous surface force (see [6]). Special care is taken to avoid spurious oscillations of pressure and generation of artificial acoustic waves in the numerical mixture layer by including specific functions of the EOS parameters as flow variables. Numerical tests are presented to verify the performance and stability properties for a wide range of flows.

**Keywords:** Compressible Navier-Stokes equations; low Mach number flows; shock capturing; interface capturing; shock waves; numerical dissipation.

---



---

*Email address:* frolov@ualberta.ca (Roman Frolov)

## 1. Introduction

In Computational Fluid Dynamics, the most general model that describes single-component flows or multicomponent flows of immiscible fluids without mass transfer is the compressible Navier-Stokes equations (compressible NSEs). The model is valid for any value of viscosity, Mach number and for any equation of state (EOS). In many applications, only specific physical effects are of importance. In this case, one can either simplify the governing equations before designing a numerical scheme (e.g. the incompressible NSEs, the Euler equations) or simply neglect the lack of efficiency of the method under certain conditions (e.g. shock capturing schemes in the limit of low Mach numbers). It allows developing a method that is specifically designed for certain types of flows and efficiently captures certain physical phenomena. However, some flows feature regions governed by different physical mechanisms, as well as various interactions between them. Studying such problems requires a universal method that is able to maintain its efficiency for a wide range of flow parameters. The objective of this paper is to propose such an algorithm.

The first challenge is the all-speed property of the scheme, i.e. the ability to simulate both nearly incompressible and compressible flows. The compressible NSEs are shown to converge to the incompressible NSEs as the Mach number ( $M$ ) goes to zero (see [7],[8]). However, numerical methods designed for highly compressible flows are known to experience severe problems in the incompressible limit (see e.g. [9],[10]), such as over-resolution in time due to the dependence of the Courant-Friedrichs-Lewy (CFL) constant on the Mach number, and over-resolution in space due to the incorrect scaling of the artificial viscosity term. Due to its importance, the issue of developing an all-speed algorithm received the significant attention of researchers from various related fields. A number of studies are dedicated to designing preconditioners in order to rescale the artificial dissipation term (see e.g. [11],[12]), which is needed for stability if central differences are used for discretization of physical fluxes, and relax the time-step limitations of the explicit schemes by equalizing the speed of convective and acoustic waves. The latter can only be accomplished by destroying the time accuracy of the solution (see [12]). If one is interested in solving time-dependent problems, some degree of implicitness in the treatment of the physical fluxes is needed. Fully-implicit methods often require expensive numerical solvers. This can be avoided by constructing an explicit-implicit flux splitting (see e.g. [13],[14],[15]). A study of stability regions for some of such schemes can be found in [16]. The type of splitting is not unique and further research on various properties of different algorithms of this class is required. An alternative way to approach this problem is to develop an efficient way of solving the fully-implicit Euler system/NSEs. Linearized block implicit (LBI) factored schemes, such as algorithms from [1], [17], [2], combine a linearization technique based on the Taylor expansion with an approximate factorization strategy. Being an extension of classical Alternating direction implicit (ADI) schemes for the case of nonlinear hyperbolic conservation laws and mixed hyperbolic-parabolic PDEs, such algorithms were found successful in a number of applications, including transonic flows (see [1] for examples). A related scheme is proposed here for full compressible NSEs based on a factorization strategy from [18], (p. 83). Although it had been reported that implicit algorithms of the ADI-type do not cure the stiffness problem at low Mach numbers (see [12]), Choi and Merkle demonstrated in [3] that the reason for the ineffectiveness of the schemes is the splitting error of the factorization, which dominates the physical

fluxes as  $M \rightarrow 0$ . In this study, a reduction strategy similar to the one used in [19] is employed to solve the issue. Since the solution requires inverting only block-tridiagonal matrices, the efficiency of the scheme remains acceptable, although it is naturally more expensive in high Mach number applications than the corresponding explicit version of the same shock-capturing scheme. For the case of Navier-Stokes equations, an implicit treatment of the terms associated with viscous stress tensor allows relaxing the time-step restrictions for high values of physical viscosity (see a discussion in [20]).

Centered-in-space discretization of physical fluxes in a system of hyperbolic conservation laws requires introducing artificial dissipation terms to avoid high-frequency oscillations due to the odd-even decoupling at low Mach numbers, and spurious oscillations across flow discontinuities for highly compressible flows. Here an artificial dissipation term similar to the one used by Guermond and Popov in [4] is added implicitly to the scheme at high Mach numbers. A nonlinear adaptive choice of artificial viscosity coefficient based on the maximum wave propagation speed in local one dimensional Riemann problems (see [21] for details) allows guaranteeing the robust behavior of the method for an arbitrary system of hyperbolic conservation laws, while being less dissipative than classical first-order schemes, such as Lax-Friedrichs. For the low Mach number regime, where shock waves are not of interest, this term needs to be rescaled to avoid over-dissipation, similar to other shock-capturing schemes (see [12], [22], [23]). Instead of using a preconditioning matrix to perform such rescaling, or introducing a fourth-order difference term, a different approach is proposed in this paper. An artificial dissipation term is designed based on a second-order difference with artificial viscosity proportional to  $h^2$ . This difference operator is applied to the conservative variable and to the product of conservative variables and corresponding Jacobians. Such combination allows one to maintain control on the kinetic energy and dump high-frequency oscillations, and thus to achieve an efficient solution for low Mach-number flows.

Finally, multicomponent flows with surface tension are considered. Among conventional methods of simulation of material interfaces are interface-capturing (see e.g. [24],[20],[25],[26],[27],[28],[5]), interface-tracking (see e.g. [29],[30]), and ghost fluid methods (see e.g. [31]). Each of these techniques has advantages and disadvantages, and was successfully used for simulation of challenging flows in many studies, such as shock-interface interaction with high density ratios of density and strong shocks. The interface-capturing technique based on the advection of the volume of fluid (VoF) function (similar to [20],[27],[5]) is chosen here alongside the interface sharpening technique from [25] for its numerical efficiency, easiness of implementation in higher dimensions, ability to automatically deal with topological changes, and possible implementations of interfacial physics (see e.g. [6]). Using a diffused interface model and conservative formulation of the governing equations requires special care to avoid spurious pressure oscillations across the interface and generation of artificial acoustic waves in the numerical mixture layer (see e.g. [5],[24]). Consistency of EOS in the mixture layer and preservation of contact discontinuity are guaranteed by the appropriate choice of flow variables and their incorporation into the computation of Jacobians and linearization procedure, as well as a special treatment of the VoF-advection equation, which is consistent with the rest of the governing equations. These results are in line with the explicit case described in [5], and provide extension of LBI factored schemes to the multicomponent case. The dissipation terms used in the paper were also found to preserve the pressure and velocity equilibrium at interfaces.

The paper is organized as follows. A new version of the LBI factored scheme with splitting error reduction is described in Section 2. Section 3 is dedicated to the artificial dissipation terms at high and low Mach numbers. It finishes the formulation of the algorithm for the single component flows. The method is further extended to the multicomponent case in Section 4. Summary of the algorithm can be found in Section 5. Numerical test cases are presented in Section 6. Section 7 provides some concluding remarks and discussions on the method and possible directions for future studies.

## 2. Linearized Block ADI Method with Splitting Error Reduction.

### 2.1. Governing Equations and Linearization.

To avoid numerical errors introduced by non-conservative schemes in presence of shock waves (see [32],[33]), the two-dimensional compressible Navier-Stokes equations in the conservation-law form are utilized here. For the single-component case the system can be written as (see [2])

$$\begin{aligned} \frac{\partial U}{\partial t} + \frac{\partial F(U)}{\partial x} + \frac{\partial G(U)}{\partial y} &= \frac{\partial V_1(U, U_x)}{\partial x} + \frac{\partial V_2(U, U_y)}{\partial x} \\ &+ \frac{\partial W_1(U, U_x)}{\partial y} + \frac{\partial W_2(U, U_y)}{\partial y} \end{aligned} \quad (1)$$

where  $U = (\rho, m, n, E)$  is the vector of conservative variables (density, momentum in x and y direction, and total energy),  $F$  and  $G$  are the fluxes associated with the Euler system, and  $V_1, V_2, W_1, W_2$  are the fluxes associated with the viscous stress tensor part (see Appendix A for details).

Using the mixed implicit-explicit Euler time discretization, one can write a semi-discrete version of (1) as

$$\begin{aligned} \frac{U^{n+1} - U^n}{\tau} + \frac{\partial F^{n+1}(U)}{\partial x} + \frac{\partial G^{n+1}(U)}{\partial y} &= \frac{\partial V_1^{n+1}(U, U_x)}{\partial x} + \frac{\partial V_2^n(U, U_y)}{\partial x} \\ &+ \frac{\partial W_1^n(U, U_x)}{\partial y} + \frac{\partial W_2^{n+1}(U, U_y)}{\partial y} \end{aligned} \quad (2)$$

where  $\tau$  is the time step. Due to the non-linearity of fluxes  $F, G, V_1$ , and  $W_2$ , a space-discretization of (2) produces a non-linear system of algebraic equations. To approximate the solution of the nonlinear system, a simple linearization, similar to the one from [1] can be employed:

$$F^{n+1} = F^n + \left( \frac{\partial F}{\partial U} \right)^n (U^{n+1} - U^n) \quad (3)$$

$$G^{n+1} = G^n + \left( \frac{\partial G}{\partial U} \right)^n (U^{n+1} - U^n) \quad (4)$$

$$V_1^{n+1} = V_1^n + \left( \frac{\partial V_1}{\partial U} \right)^n (U^{n+1} - U^n) + \left( \frac{\partial V_1}{\partial U_x} \right)^n (U_x^{n+1} - U_x^n) \quad (5)$$

$$W_2^{n+1} = W_2^n + \left( \frac{\partial W_2}{\partial U} \right)^n (U^{n+1} - U^n) + \left( \frac{\partial W_2}{\partial U_y} \right)^n (U_y^{n+1} - U_y^n). \quad (6)$$

Substituting expressions (3)-(6) into (2) and combining explicit terms and implicit terms in corresponding directions, (2) can be written as

$$(\mathbf{I} + \tau \mathbf{A}_x + \tau \mathbf{A}_y) U^{n+1} = \tau R^n \quad (7)$$

where

$$\mathbf{A}_x = \frac{\partial}{\partial x} \left( \frac{\partial F}{\partial U} \right)^n - \frac{\partial}{\partial x} \left( \frac{\partial V_1}{\partial U} \right)^n - \frac{\partial}{\partial x} \left( \frac{\partial V_1}{\partial U_x} \right)^n \frac{\partial}{\partial x} \quad (8)$$

$$\mathbf{A}_y = \frac{\partial}{\partial y} \left( \frac{\partial G}{\partial U} \right)^n - \frac{\partial}{\partial y} \left( \frac{\partial W_2}{\partial U} \right)^n - \frac{\partial}{\partial y} \left( \frac{\partial W_2}{\partial U_y} \right)^n \frac{\partial}{\partial y} \quad (9)$$

$$\begin{aligned} R^n = & \frac{1}{\tau} U^n + \frac{\partial}{\partial x} \left[ \left( \frac{\partial F}{\partial U} \right)^n U^n - F^n \right] + \frac{\partial}{\partial y} \left[ \left( \frac{\partial G}{\partial U} \right)^n U^n - G^n \right] \\ & + \frac{\partial V_2^n}{\partial x} - \frac{\partial}{\partial x} \left[ \left( \frac{\partial V_1}{\partial U} \right)^n U^n \right] - \frac{\partial}{\partial x} \left[ \left( \frac{\partial V_1}{\partial U_x} \right)^n \frac{\partial}{\partial x} U^n \right] \\ & + \frac{\partial W_1^n}{\partial y} - \frac{\partial}{\partial y} \left[ \left( \frac{\partial W_2}{\partial U} \right)^n U^n \right] - \frac{\partial}{\partial y} \left[ \left( \frac{\partial W_2}{\partial U_y} \right)^n \frac{\partial}{\partial y} U^n \right]. \end{aligned} \quad (10)$$

Folowing the approach in [18] (p.83), equation (7) can be approximated by the following factorized equation

$$(\mathbf{I} + \tau \mathbf{A}_x)(\mathbf{I} + \tau \mathbf{A}_y) U^{n+1} = \tau R^n \quad (11)$$

with the splitting error  $\mathbf{ER}(U_k^{n+1}) = \tau^2 \mathbf{A}_x \mathbf{A}_y U^{n+1}$ , and solved as a sequence of two one dimensional problems

$$(\mathbf{I} + \mathbf{A}_x) \hat{U}^{n+1} = \tau R^n \quad (12)$$

$$(\mathbf{I} + \mathbf{A}_y) U^{n+1} = \hat{U}^{n+1}. \quad (13)$$

Each of these problems only requires solving block-tridiagonal linear systems, which can be done by using an extension of the Thomas algorithm for tridiagonal systems (e.g. see [34], Volume 1, pp.188-189). The parallel implementation of the Thomas algorithm using the Schur complement technique and domain decomposition, as described in [35], can be easily extended for the block-tridiagonal version of the linear solver.

**Remark 2.1.** *The method can be reformulated for different, more accurate time-marching schemes and different splitting strategies to improve accuracy. Here the implicit Euler method with the splitting from [18], (p.83) are chosen for their simplicity and robustness. In particular, this splitting allows multicomponent factorization of non-commutative operators. Therefore, an extension of the method to the three dimensional case is possible.*

## 2.2. Splitting error reduction.

The splitting error introduced by the factorization has been found to grow as the Mach number goes to zero, while in one dimension the LBI factored schemes demonstrate a performance similar to the artificial compressibility method (see [3] for details). There are several possible ways of reducing the error (see [36] for a review). One of the possibilities is to perform the following iterative procedure until convergence

$$(\mathbf{I} + \mathbf{A}_x)\hat{U}_{k+1}^{n+1} = \tau R^n + \mathbf{ER}(U_k^{n+1}) \quad (14)$$

$$(\mathbf{I} + \mathbf{A}_y)U_{k+1}^{n+1} = \hat{U}_{k+1}^{n+1} \quad (15)$$

with  $U_0^{n+1} = U^n$ . This reduction strategy is similar to the one used in [19] in context of two-dimensional Maxwell equations.

However, none of the test cases presented in this paper required more than one iteration, i.e. simple addition of  $\mathbf{ER}(U^n)$  to the right-hand-side of the system provided sufficient reduction of the splitting error for tests with low Mach number flows. Hence, at every time step the following system was solved:

$$(\mathbf{I} + \mathbf{A}_x)\hat{U}^{n+1} = \tau R^n + \mathbf{ER}(U^n) \quad (16)$$

$$(\mathbf{I} + \mathbf{A}_y)U^{n+1} = \hat{U}^{n+1}. \quad (17)$$

No splitting error reduction was needed for tests with high Mach number flows.

Note that the proposed technique is equivalent to the preconditioned Richardson iterative method (see e.g. [37], Chapter 6) applied to the linearized system (7). Indeed, if

$$\mathbf{A} = \mathbf{I} + \tau \mathbf{A}_x + \tau \mathbf{A}_y \quad (18)$$

a preconditioner can be defined as

$$\mathbf{P} = (\mathbf{I} + \tau \mathbf{A}_x)(\mathbf{I} + \tau \mathbf{A}_y). \quad (19)$$

Then  $\mathbf{A} = \mathbf{P} - \mathbf{ER}$  where  $\mathbf{ER} = \tau^2 \mathbf{A}_x \mathbf{A}_y$ . Then, the system (14)-(15) is equivalent to

$$\mathbf{P}U_{k+1}^{n+1} = \mathbf{ER}U_k^{n+1} + \tau R^n \quad (20)$$

or alternatively

$$U_{k+1}^{n+1} = U_k^{n+1} + \mathbf{P}^{-1} \mathbf{r}_k \quad (21)$$

$$\mathbf{r}^k = \tau R^n - \mathbf{A}U_k^{n+1}. \quad (22)$$

The choice of the preconditioner allows for fast convergence of the method (one iteration in all the presented low Mach number tests).

### 3. Stabilization.

#### 3.1. Guermond-Popov shock-capturing scheme.

A finite-element numerical method for general hyperbolic systems, proposed in [4], can be reformulated in terms of finite differences/finite volumes in the standard form

$$\frac{U_{i,j}^{n+1} - U_{i,j}^n}{\tau} + \frac{\hat{F}_{i+\frac{1}{2},j}^n - \hat{F}_{i-\frac{1}{2},j}^n}{h_x} + \frac{\hat{G}_{i,j+\frac{1}{2}}^n - \hat{G}_{i,j-\frac{1}{2}}^n}{h_y} = 0 \quad (23)$$

with numerical numerical fluxes

$$\hat{F}_{i+\frac{1}{2},j}^n = \frac{F_{i+1,j}^n + F_{i,j}^n}{2} - d_{i+1,j} (U_{i+1,j}^n - U_{i,j}^n). \quad (24)$$

Artificial viscosity coefficients are defined here as

$$d_{i+1,j} = \frac{1}{h_x} \lambda_{max}(U_{i+1,j}^n, U_{i,j}^n) \quad (25)$$

with  $\lambda_{max}(U_l, U_r)$  being a maximum wave speed estimation for the corresponding local one dimensional Riemann problem with initial conditions given by  $U_l$  and  $U_r$  (see [4],[21] for details), and  $h_x$  being a space step in  $x$ -direction.

The original algorithm is fully explicit and preserves all the convex invariant sets, which, in the case of the Euler system, guarantees positivity of density and internal energy, and produces a solution that satisfies entropy inequality for every entropy pair of the hyperbolic system (see [4] for details). These properties are essential for obtaining an approximation of a physical solution for the Euler equations and are achieved without any extra constructions (such as flux limiters or non-oscillatory reconstructions). Unlike Godunov-type schemes, the method does not require an exact or approximate solution of local Riemann problems. Only an estimation of the maximum speed of wave propagation is needed. The efficiency of the algorithm depends on a particular method used to obtain the estimation. The estimation procedure proposed in this study can be found in Section 4.5. The procedure is developed for the case of multiple components obeying Stiffened Gas EOS and includes the effects of surface tension.

**Remark 3.1.** *If  $\lambda_{max}(U_l, U_r) = \frac{h}{4\tau}$ , the method reproduces the classical Lax-Friedrichs scheme. Due to the nonlinear definition of  $\lambda_{max}$  through the maximum wave speed of local one dimensional Riemann problems, the Guermond-Popov (GP) method achieves the same level of robustness as the Lax-Friedrichs (LF) scheme while maintaining much sharper flow discontinuities (see Section 6.2 for comparison).*

As can be easily seen by substituting the expression (24) into the equation (23), the method adds a second-order artificial dissipation term of the type (GP-dissipation term)

$$\begin{aligned} \mathbf{D}^{GP}U = & [d_{i+1,j}U_{i+1,j} + d_{i-1,j}U_{i-1,j} \\ & + d_{i,j+1}U_{i,j+1} + d_{i,j-1}U_{i,j-1} \\ & - (d_{i+1,j} + d_{i-1,j} + d_{i,j+1} + d_{i,j-1})U_{i,j}] \end{aligned} \quad (26)$$

to the original explicit centered-in-space scheme. The same second-order stabilizing term

can be added to the implicit scheme for the compressible NSEs in the high Mach number regime; which is equivalent to defining the inviscid fluxes as

$$\hat{F}_{i+\frac{1}{2},j}^{n+1} = \frac{F_{i+1,j}^{n+1} + F_{i,j}^{n+1}}{2} - d_{i+1,j} (U_{i+1,j}^{n+1} - U_{i,j}^{n+1}) \quad (27)$$

and applying the same linearization and factorization procedures after that. This implicit treatment of the dissipation term does not disrupt the block-tridiagonal nature of the resulting linear system and therefore does not increase the cost of the computations.

### 3.2. Damping of high-frequency oscillations.

Like other artificial dissipation terms designed for stabilization around strong shocks,  $\mathbf{D}^{GP}U$  starts dominating the physical solution as the Mach number goes to zero. Indeed, in the incompressible limit (where the velocity of the flow is small comparing to the speed of sound,  $|u| \ll c$ ) the maximum wave speed  $\lambda_{max} = u \pm c \sim c$ . The perturbed Euler system in one dimension can be written as

$$\frac{\partial \rho}{\partial t} + \frac{\partial}{\partial x}(\rho u) - h \frac{\partial}{\partial x} \lambda \frac{\partial}{\partial x} \rho = 0 \quad (28)$$

$$\frac{\rho u}{\partial t} + \frac{\partial}{\partial x}(\rho u^2 + p) - h \frac{\partial}{\partial x} \lambda \frac{\partial}{\partial x} \rho u = 0 \quad (29)$$

$$\frac{E}{\partial t} + \frac{\partial}{\partial x}((E + p)u) - h \frac{\partial}{\partial x} \lambda \frac{\partial}{\partial x} E = 0. \quad (30)$$

Then, introducing the characteristic scales: length ( $L$ ), density ( $\tilde{\rho}$ ), and velocity ( $\tilde{U}$ ), dimensionless variables can be defined as

$$x^* = \frac{x}{L} \quad (31)$$

$$\rho^* = \frac{\rho}{\tilde{\rho}} \quad (32)$$

$$u^* = \frac{u}{\tilde{U}} \quad (33)$$

$$t^* = \frac{t}{\tilde{U}/L} \quad (34)$$

$$M = \frac{\tilde{U}}{c} \quad (35)$$

$$p^* = \frac{p}{\tilde{\rho} c^2} \quad (36)$$

$$E^* = \frac{E}{\tilde{\rho} c^2}. \quad (37)$$



Since  $\lambda \sim c$ , the system can be rewritten in the following non-dimensional form

$$\frac{\partial \rho^*}{\partial t^*} + \frac{\partial}{\partial x^*}(\rho^* u^*) - \frac{h}{M} \frac{\partial^2}{(\partial x^*)^2} \rho^* = 0 \quad (38)$$

$$\frac{\rho^* u^*}{\partial t^*} + \frac{\partial}{\partial x^*} \left( \rho^* (u^*)^2 + \frac{p^*}{M^2} \right) - \frac{h}{M} \frac{\partial^2}{(\partial x^*)^2} \rho^* u^* = 0 \quad (39)$$

$$\frac{E}{\partial t^*} + \frac{\partial}{\partial x^*} ((E^* + p^*) u^*) - \frac{h}{M} \frac{\partial^2}{(\partial x^*)^2} E^* = 0. \quad (40)$$

Hence, the artificial dissipation term indeed becomes dominant as  $M \rightarrow 0$  if  $h$  is fixed.

At low Mach number, the following dissipation term is proposed in this paper (Low Mach (LM) dissipation term):

$$\begin{aligned} \mathbf{D}^{LM} U^{n+1} &= \mathbf{D}_1^{LM} U^{n+1} + \mathbf{D}_2^{LM} U^{n+1} = \\ &h^2 \omega_1 \nabla^2 U^{n+1} + h^2 \omega_2 \left( \frac{\partial^2}{\partial x^2} \left[ \left( \frac{\partial F}{\partial U} \right)^n U^{n+1} \right] + \frac{\partial^2}{\partial y^2} \left[ \left( \frac{\partial G}{\partial U} \right)^n U^{n+1} \right] \right) \end{aligned} \quad (41)$$

where  $\omega_1$  and  $\omega_2$  are scalar dimensionless parameters.

The purpose of the first term here (which is the same as the GP-term with  $\lambda \equiv h$ ) is to drain off the kinetic energy and thus maintain the overall stability of the computations. The second and the third terms are used to regularize the entries of the corresponding matrix operator, and connect odd and even nodes which are decoupled due to the use of centered-in-space discretization for hyperbolic fluxes. Jacobians provide proper weights for every variable depending on the magnitude of its contribution to the linearized flux. The effects of both of these terms at different values of the Mach number are illustrated by numerical examples in Section 6.1.

**Remark 3.2.** *A related idea of matching the scaling of the artificial viscosity matrix with the scaling of the Jacobians in order to stabilize the system in the low Mach number limit was used in [22] in the context of Roe-Turkel scheme. However, here instead of choosing scaling parameters to match orders of magnitude of the Jacobian's components, these components themselves are used in the stabilizing term. This was found to be more efficient in the context of the present scheme. Furthermore, as it is revealed in the Section 4.2, the artificial dissipation term does not disrupt the velocity and pressure equilibrium at interfaces.*

As for the GP-dissipation term, the LM-term can be incorporated into the factorization strategy in a straightforward way with direction splitting. Since the splitting error due to the LM term involves the components of the Jacobian, it should be taken into account while performing the reduction strategy described above.

If flow features regions of low and high Mach numbers, switching between LM and GP dissipation terms can be performed based on the local Mach number  $M_{loc}$  in the following way

$$\mathbf{D} U^{n+1} = k^{(HM)} \mathbf{D}^{GP} U^n + k^{(LM)} \mathbf{D}^{LM} U^n \quad (42)$$

where  $k^{(HM)}$ ,  $k^{(LM)}$ ,  $\omega_1$ , and  $\omega_2$  are scalar dimensionless parameters to be defined. Using an approximation to the Heaviside step-function and setting a threshold Mach number  $M_{tr}$ ,  $k^{(HM)}$  and  $k^{(LM)}$  are defined as

$$k^{(HM)} = \frac{1}{1 + e^{-2k(M_{loc} - M_{tr})}}. \quad (43)$$

$$k^{(LM)} = 1 - k^{(2)}. \quad (44)$$

The described strategy has been shown to be efficient for Mach numbers as low as  $M = 10^{-6}$ . See Section 6.1 for details and numerical illustrations.

**Remark 3.3.** *The parameters  $\omega_1$  and  $\omega_2$  still have to be tuned manually depending on the particular application. A rigorous, theoretically justified adaptive scaling of these artificial viscosity coefficients may be a significant improvement to the algorithm.*

Hence, the operators  $\mathbf{A}_x$  and  $\mathbf{A}_y$  from (8) and (9) are redefined to include the implicit artificial dissipation terms as follows

$$\mathbf{A}_x = \frac{\partial}{\partial x} \left( \frac{\partial F}{\partial U} \right)^n - \frac{\partial}{\partial x} \left( \frac{\partial V_1}{\partial U} \right)^n - \frac{\partial}{\partial x} \left( \frac{\partial V_1}{\partial U_x} \right)^n \frac{\partial}{\partial x} - \mathbf{D}_x \quad (45)$$

$$\mathbf{A}_y = \frac{\partial}{\partial y} \left( \frac{\partial G}{\partial U} \right)^n - \frac{\partial}{\partial y} \left( \frac{\partial W_2}{\partial U} \right)^n - \frac{\partial}{\partial y} \left( \frac{\partial W_2}{\partial U_y} \right)^n \frac{\partial}{\partial y} - \mathbf{D}_y \quad (46)$$

where  $\mathbf{D}_x$  and  $\mathbf{D}_y$  are parts of the dissipation term  $\mathbf{D}U^{n+1}$ , defined by (42), consisting of finite differences in corresponding directions.

#### 4. Interface Capturing and Computation of the Surface Tension.

The interface capturing approach is based on the solution of the advection equation for the volume of fluid (VoF) function  $\phi$  (see [24],[5],[26],[27],[28],[20] for examples of applications, and discussions on the method).

$$\frac{\partial \phi}{\partial t} + \vec{u} \cdot \nabla \phi = 0 \quad (47)$$

where  $\vec{u} = (\frac{m}{\rho}, \frac{n}{\rho}) = (u, v)$  is the flow velocity.

Initially,  $\phi$  is set to 1 for the first fluid, and 0 for the second one. Due to numerical diffusion, this initial discontinuity becomes smoothed out which forms an artificial mixing layer where  $\phi \in (0, 1)$ . EOS parameters have to be consistently defined in the layer to avoid spurious pressure oscillations, which appear when a conservative model is employed (see e.g. [24],[28],[27],[33]). Here, Stiffened Gas EOS (SG EOS) is used (see [38]):

$$p = (\gamma - 1)\rho e - \gamma\pi_\infty \quad (48)$$

where  $\gamma$  and  $\pi_\infty$  are constants for a given fluid,  $e$  is the internal energy, defined implicitly through

$$E = \rho e + \rho \frac{u^2 + v^2}{2}. \quad (49)$$

SG EOS is commonly used to model compressible multicomponent flows of gases, liquids, and solids (e.g. air, water, copper, uranium) (see [20] for details). Note that the ideal gas EOS is a particular case of the SG EOS with  $\pi_\infty = 0$ .

#### 4.1. Barotropic Mixture Laws.

If  $\rho_i$ ,  $e_i$ ,  $p_i$  ( $i = 1, 2$ ) are density, internal energy and pressure for corresponding fluids, then

$$\rho = \phi\rho_1 + (1 - \phi)\rho_2 \quad (50)$$

$$\rho e = \phi\rho_1 e_1 + (1 - \phi)\rho_2 e_2 \quad (51)$$

$$p = \phi p_1 + (1 - \phi)p_2. \quad (52)$$

In the regions of pure fluid 1 or pure fluid 2, pressure is given by the EOS (48). In the artificial mixing layer, where both components are present, the following condition must be satisfied (see [24])

$$p_1 = p_2 = p. \quad (53)$$

Then

$$\begin{aligned} \rho e = & \phi \frac{p + \gamma_1 \pi_1}{\gamma_1 - 1} + (1 - \phi) \frac{p + \gamma_2 \pi_2}{\gamma_2 - 1} = \\ & p \left( \frac{\phi}{\gamma_1 - 1} + \frac{1 - \phi}{\gamma_2 - 1} \right) + \left( \frac{\phi \gamma_1 \pi_1}{\gamma_1 - 1} + \frac{(1 - \phi) \gamma_2 \pi_2}{\gamma_2 - 1} \right) \end{aligned} \quad (54)$$

which leads to the following definition of the proper averaging for the EOS coefficients in the mixing layer ( $\gamma$ ,  $\pi^\infty$ )

$$\alpha = \frac{1}{1 - \gamma} = \phi \frac{1}{1 - \gamma_1} + (1 - \phi) \frac{1}{1 - \gamma_2} \quad (55)$$

$$\beta = \frac{\pi^\infty \gamma}{1 - \gamma} = \phi \frac{\pi_1^\infty \gamma_1}{1 - \gamma_1} + (1 - \phi) \frac{\pi_2^\infty \gamma_2}{1 - \gamma_2}. \quad (56)$$

Further considerations will reveal an important role of the parameters  $\alpha$  and  $\beta$ .

#### 4.2. Preservation of contact discontinuities.

Another requirement needed to preserve the pressure and velocity equilibrium in multicomponent flows is that if the velocity and pressure are constants at time  $t^n$  they remain constants at  $t^{n+1}$  (preservation of a contact discontinuity) (see [5] for details).

$$\text{if } u_i^{(1)} = u \text{ and } p_i^{(1)} = p \text{ for any } i, \text{ then } u_i^{(2)} = u \text{ and } p_i^{(2)} = p$$

To avoid technicalities, the one dimensional inviscid case will be considered here. The following analysis can be easily extended to the multidimensional case. The viscous part of the equations does not disrupt the velocity and pressure equilibrium, since it only involves terms with velocity derivatives.

Here, a strategy similar to [5] is used to verify that the proposed method preserves contact discontinuities, i.e. if  $u_i^{(n)} = u$  and  $p_i^{(n)} = p$  for any  $i$ , then  $u_i^{(n+1)} = u$  and  $p_i^{(n+1)} = p$ . For a one dimensional inviscid flow, the system (11) becomes

$$\begin{aligned} U^{n+1} + \tau \frac{\partial}{\partial x} \left[ \left( \frac{\partial F}{\partial U} \right)^n U^{n+1} \right] = & U^n + \tau \frac{\partial}{\partial x} \left[ \left( \frac{\partial F}{\partial U} \right)^n U^n - F^n \right] \\ & + \tau D_1(U^{n+1}) + \tau D_2(U^{n+1}) + \tau D_3(U^{n+1}) \end{aligned} \quad (57)$$

where

$$D_1(U^{n+1}) = h \frac{\partial}{\partial x} \lambda \frac{\partial}{\partial x} U^{n+1} \quad (58)$$

$$D_2(U^{n+1}) = h^2 \frac{\partial^2}{\partial x^2} U^{n+1} \quad (59)$$

$$D_3(U^{n+1}) = h^2 \frac{\partial^2}{\partial x^2} \left( \frac{\partial F}{\partial U} \right)^n U^{n+1}. \quad (60)$$

Here, only mass, momentum and energy equations are considered. As it will become clear later, the preservation of contact discontinuities enforces that the use of  $\alpha$  and  $\beta$  as variables (i.e. the set of variables  $U = (\rho, m, E)$  has to be extended as  $U = (\rho, m, E, \alpha, \beta) = (\rho, \rho u, \frac{\rho u^2}{2} + \beta + \alpha p, \alpha, \beta)$ ) and restricts the choice of a numerical method for the advection equation (47).

Given that  $u_i^{(n)} = u$  and  $p_i^{(n)} = p$ , it is assumed that the same holds at the next time level, i.e.  $u_i^{(n+1)} = u$  and  $p_i^{(n+1)} = p$ . This assumption is used to simplify (57). Then, if (57) is consistent, the assumption is proven to be true, and no disturbances of pressure and velocity are introduced at  $t^{n+1}$ , and the method preserves contact discontinuities.

Using Appendix A

$$F^n = \begin{bmatrix} \rho^n u & \rho^n u^2 + p & \frac{\rho^n u^3}{2} + u\beta^n + up\alpha^n + up \end{bmatrix}^T \quad (61)$$

$$\left( \frac{\partial F}{\partial U} \right)^n = \begin{bmatrix} 0 & 1 & 0 & 0 & 0 \\ -u^2 + \frac{u^2}{2\alpha^n} & 2u - \frac{u}{\alpha^n} & \frac{1}{\alpha^n} & \frac{p}{\alpha^n} & -\frac{1}{\alpha^n} \\ \delta_1 & \delta_2 & u(1 + \frac{1}{\alpha^n}) & -\frac{up}{\alpha^n} & -\frac{u}{\alpha^n} \end{bmatrix} \quad (62)$$

$$\text{where } \delta_1 = -\frac{(\alpha^n p + p + \beta^n + \frac{\rho^n u^2}{2})u}{\rho^n} + \frac{u^3}{2\alpha^n}, \delta_2 = \frac{\alpha^n p + p + \beta^n + \frac{\rho^n u^2}{2}}{\rho^n} - \frac{u^2}{\alpha^n}.$$

$$\left( \frac{\partial F}{\partial U} \right)^n U^n = \begin{bmatrix} u\rho^n & u^2\rho^n & \frac{u^3\rho^n}{2} + u\beta^n + up\alpha^n \end{bmatrix}^T \quad (63)$$

$$\left( \frac{\partial F}{\partial U} \right)^n U^{n+1} = \begin{bmatrix} u\rho^{n+1} & u^2\rho^{n+1} & \frac{u^3\rho^{n+1}}{2} + u\beta^{n+1} + up\alpha^{n+1} \end{bmatrix}^T. \quad (64)$$

Hence,

$$\left( \frac{\partial F}{\partial U} \right)^n U^n - F^n = \begin{bmatrix} 0 & -p & -up \end{bmatrix}^T \quad (65)$$

and

$$\frac{\partial}{\partial x} \left[ \left( \frac{\partial F}{\partial U} \right)^n U^n - F^n \right] = \begin{bmatrix} 0 & 0 & 0 \end{bmatrix}^T. \quad (66)$$

Using (63), the mass conservation equation in a discrete form reads as

$$\rho_i^{n+1} + \tau u \frac{\rho_{i+1}^{n+1} - \rho_{i-1}^{n+1}}{h} - \rho_i^n - D_1(\rho^{n+1}) - D_2(\rho^{n+1}) - u D_3(\rho^{n+1}) = 0, \quad (67)$$

the momentum conservation

$$\begin{aligned}
& \rho_i^{n+1}u + \tau u^2 \frac{\rho_{i+1}^{n+1} - \rho_{i-1}^{n+1}}{h} - \rho_i^n u - D_1(\rho^{n+1}u) - D_2(\rho^{n+1}u) \\
& \quad - uD_3(\rho^{n+1}u) = \\
& u \left( \rho_i^{n+1} + \tau u \frac{\rho_{i+1}^{n+1} - \rho_{i-1}^{n+1}}{h} - \rho_i^n - D_1(\rho^{n+1}) - D_2(\rho^{n+1}) \right. \\
& \quad \left. - uD_3(\rho^{n+1}) \right) = 0,
\end{aligned} \tag{68}$$

which is satisfied if (67) is. Hence, the mass and momentum conservation parts of (57) are consistent under the assumption of preservation of contact discontinuities. It was achieved by including  $\alpha$  and  $\beta$  into the set of conservative variables.

Energy equation can be written as

$$\begin{aligned}
& E^{n+1} + \tau u \left( \frac{\rho_{i+1}^{n+1}u^2 - \rho_{i-1}^{n+1}u^2}{2h} + \frac{\beta_{i+1}^{n+1} - \beta_{i-1}^{n+1}}{h} + p \frac{\alpha_{i+1}^{n+1} - \alpha_{i-1}^{n+1}}{h} \right) \\
& \quad - E^n - D_1(E^{n+1}) - D_2(E^{n+1}) - D_3(E^{n+1}) = 0
\end{aligned} \tag{69}$$

expressing energy through the EOS as  $E = \alpha p + \frac{u^2}{2}\rho + \beta$ , and substituting it into the previous equations allows one to rewrite it as

$$\begin{aligned}
& \frac{u^2}{2} \left( \rho_i^{n+1} + \tau u \frac{\rho_{i+1}^{n+1} - \rho_{i-1}^{n+1}}{h} - \rho^n - D_1(\rho^{n+1}) - D_2(\rho^{n+1}) - \right. \\
& \quad \left. uD_3(\rho^{n+1}) \right) + \\
& p \left( \alpha_i^{n+1} + \tau u \frac{\alpha_{i+1}^{n+1} - \alpha_{i-1}^{n+1}}{h} - \rho^n - D_1(\alpha^{n+1}) - D_2(\alpha^{n+1}) \right. \\
& \quad \left. - uD_3(\alpha^{n+1}) \right) \\
& + \left( \beta_i^{n+1} + \tau u \frac{\beta_{i+1}^{n+1} - \beta_{i-1}^{n+1}}{h} - \beta^n - D_1(\beta^{n+1}) - D_2(\beta^{n+1}) \right. \\
& \quad \left. - uD_3(\beta^{n+1}) \right) = 0.
\end{aligned} \tag{70}$$

The first term here is zero if the mass equation (67) is satisfied. The second and third terms in (70) dictate the choice of numerical discretization for the interfacial advection equation. These two terms represent discrete forms of the advection of  $\alpha$  and  $\beta$ , i.e.

$$\frac{\partial \alpha}{\partial t} + \vec{u} \cdot \nabla \alpha = 0 \tag{71}$$

and

$$\frac{\partial \beta}{\partial t} + \vec{u} \cdot \nabla \beta = 0 \quad (72)$$

The particular form of their discretization in (70) follows from the discretization of the energy equation. Hence, in order to guarantee cancellation of the last two terms in (70) and thus preserve contact discontinuities, (71) and (72) have to be discretized in a way consistent with the rest of the system. In particular it must be consistent with the energy equation, e.g.

$$\begin{aligned} \frac{\alpha_i^{n+1} - \alpha_i^n}{\tau} + u^n \frac{\alpha_{i+1}^{n+1} - \alpha_{i-1}^{n+1}}{h} - D_1(\alpha^{n+1}) - D_2(\alpha^{n+1}) \\ - D_3(u^n \alpha^{n+1}) = 0 \end{aligned} \quad (73)$$

$$\begin{aligned} \frac{\beta_i^{n+1} - \beta_i^n}{\tau} + u^n \frac{\beta_{i+1}^{n+1} - \beta_{i-1}^{n+1}}{h} - D_1(\beta^{n+1}) - D_2(\beta^{n+1}) \\ - D_3(u^n \beta^{n+1}) = 0. \end{aligned} \quad (74)$$

This analysis can be trivially extended to the multidimensional case, where the same argument leads to the use of the same factorization and splitting error reduction strategies for the interfacial advection as for the rest of the system.

Hence, similarly to the Godunov-Rusanov scheme from [5], the contact discontinuity preservation condition dictates how the advection of the VoF function has to be solved. It forces one to use the same time-marching algorithm, factorization strategy, same splitting error reduction technique (if it is needed), and the same artificial dissipation term for the advection (47) as one does for the energy conservation equation. Besides, the analysis reveals that the parameters  $\alpha$  and  $\beta$  have to be included in the set of conservative variables and be taken into account while constructing the Jacobians and performing the linearization.

However, solving two similar advection equations for both  $\alpha$  and  $\beta$  can be avoided. Indeed, they both follow from the solution of (47) and (55)-(56). Linearized and discretized version of (47) reads as

$$\frac{\phi^{n+1} - \phi^n}{\tau} - \vec{u}^n \cdot \nabla_h \phi^{n+1} = 0 \quad (75)$$

where  $\nabla_h$  is a centered-difference approximation of the gradient operator.  $\phi^{n+1}$  can be found from (75) before updating other variables and used to compute  $\alpha^{n+1}$  and  $\beta^{n+1}$ . It allows one to compute their contributions to the remaining system as a part of the right-hand-sides of (12)-(13).

In the most general case, the VoF function is updated through an iterative (until the overall splitting error is reduced enough) solution of

$$(\mathbf{I} + \tau u^n \partial_x - \tau \mathbf{D}_x) \hat{\phi}_{k+1}^{n+1} = \phi^n + \mathbf{ER}(\phi_k^{n+1}) \quad (76)$$

$$(\mathbf{I} + \tau v^n \partial_y - \tau \mathbf{D}_y) \hat{\phi}_{k+1}^{n+1} = \hat{\phi}^{n+1} \quad (77)$$

where

$$\mathbf{ER}(\phi_k^{n+1}) = \tau^2 (u^n \partial_x - \mathbf{D}_x)(v^n \partial_y - \mathbf{D}_y). \quad (78)$$

#### 4.3. Interface sharpening.

Interface-capturing schemes are known to diffuse interfaces during the course of computations, due to the introduction of artificial dissipation. A sharpening algorithm is proposed in [25] to keep the width of the interface constant (typically several grid cells). To achieve this,  $\rho$  and  $\phi$  are updated by solving the following artificial compression equations iteratively using the central difference approximation until the steady state is reached (with some predefined tolerance  $tol$ ):

$$\frac{\partial \rho}{\partial T} = H(\phi) \vec{n} \cdot (\nabla (\epsilon_h \vec{n} \cdot \nabla \rho) - (1 - 2\phi) \nabla \rho) \quad (79)$$

$$\frac{\partial \phi}{\partial T} = \vec{n} \cdot (\epsilon_h |\nabla \phi| - \phi(1 - \phi)) \quad (80)$$

where  $T$  is an artificial time-like parameter,  $\epsilon_h$  is the parameter which controls the thickness of the interface, and

$$H(\phi) = \tanh\left(\left(\frac{\phi(1 - \phi)}{10^{-2}}\right)^2\right), \quad (81)$$

which limits the artificial compression in the interfacial layer and prevents the density update to influence other types of discontinuities, such as shock waves.

The parameter  $\epsilon_h$  is typically chosen to be proportional to the grid size, as  $\epsilon_h = \epsilon \cdot h$ , where  $\epsilon$  is a scalar dimensionless parameter to be defined for each particular application. The algorithm has been shown to be robust and efficient, even for high density ratios.

A relatively sharp interfacial profile is maintained, and the accuracy of the computation of interface normals suffers from numerical artifacts, since it involves the calculation of the gradient of the function  $\phi$ . [25] introduces the following function

$$\psi = \frac{\phi^\alpha}{\phi^\alpha + (1 - \phi)^\alpha}, \alpha < 1 \quad (82)$$

to calculate the interface normal vector as

$$\mathbf{n} = \frac{\nabla \phi}{|\nabla \phi|} = \frac{\nabla \psi}{|\nabla \psi|}. \quad (83)$$

Due to the smoother profile of  $\psi$ , the accuracy of the computations is increased.

#### 4.4. Surface tension effects.

One of the advantages of the interface-capturing approach is a relatively straightforward implementation of surface tension interfacial effects, which can be incorporated into the model by adding a continuous surface force (CSF) explicitly to the governing equation. [6] proposes two possible approaches, non-conservative and conservative formulations of the CSF.

The first approach adds the following contributions to the momentum and energy equations (assuming that  $\phi = 1$  for the liquid phase,  $\phi = 0$  for the gas phase).

$$F_m^{ST} = \sigma \kappa \nabla \phi \quad (84)$$

$$F_E^{ST} = \sigma \kappa \vec{u} \cdot \nabla \phi \quad (85)$$

where  $\sigma [\frac{N}{m}]$  is the surface tension coefficient,  $\kappa = -\nabla \cdot \frac{\nabla \phi}{|\nabla \phi|}$  is the interfacial curvature.

An alternative way is to redefine the total energy by including a term associated with the interfacial energy

$$\hat{E} = E + \sigma |\nabla \phi| \quad (86)$$

and write the CSF as

$$F_m^{ST} = -\nabla \cdot \left( -\sigma \left( |\nabla \phi| \mathbf{I} - \frac{\nabla \phi \otimes \nabla \phi}{|\nabla \phi|} \right) \right) \quad (87)$$

$$F_E^{ST} = -\nabla \cdot \left( -\sigma \left( |\nabla \phi| \mathbf{I} - \frac{\nabla \phi \otimes \nabla \phi}{|\nabla \phi|} \right) \cdot \vec{u} \right). \quad (88)$$

The authors of [6] claim that the conservative approach (i.e. equation (87), and (88)) may lead to an attenuation of parasitic currents (see [39],[40]), however other researchers (see [41]) associate parasitic currents with curvature computations and related errors, rather than a surface tension model. A comparison of different CSF models and curvature approximations in the context of the present numerical method is outside of the scope of this paper.

In this study, the non-conservative approach is used, and the interfacial curvature is computed based on the interfacial normal defined by (83) and centered-in-space discretization.

**Remark 4.1.** *The present method allows a simple extension: the CSF can be added implicitly (in the conservative or non-conservative formulation) as another flux and linearized in a similar way as all the other fluxes in (2). It may be expected that such implicitness in the computation of CSF may help to relax the CFL conditions associated with capillary effects, which is of the type  $\tau \leq \text{const} \cdot \left(\frac{h^3}{\sigma}\right)^{\frac{1}{2}}$  (see [41]).*

Thus, the source term from (10) is redefined after including the surface tension as an explicit CSF as

$$\begin{aligned} R^n = & \frac{1}{\tau} U^n + \frac{\partial}{\partial x} \left[ \left( \frac{\partial F}{\partial U} \right)^n U^n - F^n \right] + \frac{\partial}{\partial y} \left[ \left( \frac{\partial G}{\partial U} \right)^n U^n - G^n \right] \\ & + \frac{\partial V_2^n}{\partial x} - \frac{\partial}{\partial x} \left[ \left( \frac{\partial V_1}{\partial U} \right)^n U^n \right] - \frac{\partial}{\partial x} \left[ \left( \frac{\partial V_1}{\partial U_x} \right)^n \frac{\partial}{\partial x} U^n \right] \\ & + \frac{\partial W_1^n}{\partial y} - \frac{\partial}{\partial y} \left[ \left( \frac{\partial W_2}{\partial U} \right)^n U^n \right] - \frac{\partial}{\partial y} \left[ \left( \frac{\partial W_2}{\partial U_y} \right)^n \frac{\partial}{\partial y} U^n \right] \\ & + F^{ST} \end{aligned} \quad (89)$$

where

$$F^{ST} = \begin{bmatrix} 0 & \sigma \kappa \partial_x \phi & \sigma \kappa \partial_y \phi & \sigma \kappa u \partial_x \phi + \sigma \kappa v \partial_y \phi & 0 & 0 \end{bmatrix}^T. \quad (90)$$



#### 4.5. Maximum Speed estimation for the multicomponent Stiffened Gas EOS.

The Guermond-Popov shock-capturing algorithm requires an estimation from above of the maximum speed of propagation in local one dimensional Riemann problems. The procedure proposed in [21] has to be modified for the multicomponent case when both fluids obey the SG EOS, and the interfacial jump in pressure due to the interfacial curvature and surface tension is present. Suppose the following parameters are given:  $(\rho_l, u_l, e_l, p_l, \gamma_l, \pi_l^\infty, \phi_l)$  and  $(\rho_r, u_r, e_r, p_r, \gamma_r, \pi_r^\infty, \phi_r)$ , and each of them obeys the EOS:

$$p_z = (\gamma_z - 1)\rho_z e_z - \gamma_z \pi_z^\infty \quad (91)$$

where  $z = l/r$ . The speed of sound can be computed as

$$c_z = \sqrt{\frac{\gamma_z(p_z + \pi_z^\infty)}{\rho_z}}. \quad (92)$$

The following one dimensional Riemann problem is considered (see [21] for details)

$$\partial_t U + \partial_x (F(U) \cdot \mathbf{n}) = 0 \quad (93)$$

where  $\mathbf{n}$  is a unit vector normal to a face of a finite volume cell, with the piecewise constant initial conditions described above. The problem is strictly hyperbolic and the solution consists of two genuinely nonlinear waves (shock or rarefaction) and one linearly degenerate middle wave (contact discontinuity) connecting left and right initial states (see [42], Chapter 4 for details). The VoF function  $\phi$  is assumed to have zero jumps across shock and rarefaction waves, and contact discontinuities. If  $\lambda_1^-$  and  $\lambda_3^+$  are two extreme wave speeds, a maximum speed of wave propagation is defined as

$$\lambda_{max} = \max((\lambda_1^-)_-, (\lambda_3^+)_+) \quad (94)$$

where  $(\lambda_1^-)_- = \max(0, -\lambda_1^-)$ ,  $(\lambda_3^+)_+ = \max(0, \lambda_3^+)$ . This is the quantity used in the GP dissipation term.

Denoting intermediate pressures by  $p_l^*$  and  $p_r^*$ , the following interfacial condition must be satisfied

$$p_r^* = p_l^* + \kappa \sigma \quad (95)$$

where  $\kappa = -\nabla \cdot \frac{\nabla \phi}{|\nabla \phi|}$  is the interfacial curvature. The case of  $\sigma = 0$  is considered first, then an extension of the proposed solution for nonzero values of  $\sigma$  is discussed.

Similar to the ideal gas case, described in [42], Chapter 4, the function

$$\eta(p) = f_l(p) + f_r(p) + u_r - u_l \quad (96)$$

is considered, where  $f_z$  is a shock curve if  $p \geq p_z$

$$f_z(p) = (p - p_z) \sqrt{\frac{2}{(\gamma_z + 1)\rho_z}} \left( p + \frac{\gamma_z - 1}{\gamma_z + 1} p_z + \frac{\gamma_z}{\gamma_z + 1} \pi_z^\infty \right)^{-\frac{1}{2}} \quad (97)$$

and a rarefaction curve otherwise (see [43])

$$f_z(p) = \frac{2c_z}{\gamma - 1} \left( \left( \frac{p + \pi_z^\infty}{p_z + \pi_z^\infty} \right)^{\frac{\gamma_z - 1}{2\gamma_z}} - 1 \right) \quad (98)$$

with  $z = l/r$ .

An intermediate pressure  $p_l^* = p_r^* = p^*$  is given then as a solution of (see [42], Chapter 4)

$$\eta(p^*) = 0. \quad (99)$$

If it is solved for  $p^*$ , then

$$\lambda_1^- = u_l - c_l \quad (100)$$

$$\lambda_3^+ = u_r + c_r \quad (101)$$

for rarefaction waves, and

$$\lambda_1^- = u_l - \frac{Q_l}{\rho_l} \quad (102)$$

$$\lambda_3^+ = u_r + \frac{Q_r}{\rho_r} \quad (103)$$

for shocks, where  $Q_z$  are the corresponding mass fluxes,

$$Q_z = \sqrt{\frac{(p^* + \frac{\gamma-1}{\gamma+1}p_z + \frac{\gamma}{\gamma+1}\pi_z^\infty)(\gamma_z + 1)\rho_z}{2}}. \quad (104)$$

Finally,

$$\lambda_{max} = \max((\lambda_1^-)_-, (\lambda_3^+)_+). \quad (105)$$

Now, since both  $f_l$  and  $f_r$  are monotonically increasing and concave down, the Newton-Secant method can be used to solve (99) for  $p^*$ . Given  $p_n^1 < p^* < p_n^2$  one can compute

$$p_{n+1}^1 = p_n^1 - \frac{\eta(p_n^1)}{\eta'(p_n^1)} \quad (106)$$

$$p_{n+1}^2 = p_n^2 - \eta(p_n^2) \frac{p_n^2 - p_n^1}{\eta(p_n^2) - \eta(p_n^1)} \quad (107)$$

until convergence. The procedure gives the estimation of  $p^*$  from above and below, which is used to estimate the maximum speed of propagation.

Shocks and rarefaction waves can be distinguished using the signs of  $\eta(p_l)$  and  $\eta(p_r)$  (positive for rarefaction waves, negative for shock waves). If the corresponding wave is a rarefaction wave,  $p^*$  is not needed for the speed estimation and the iterative process can be skipped by immediately computing the corresponding wave speed.

Assuming now a non-zero  $\sigma$ , (96) can be reformulated as

$$f_l(p_l^*) + f_r(p_r^*) + u_r - u_l = 0 \quad (108)$$

which needs to be solved in terms of one of the pressures, then the other one can be computed using (95) if needed (i.e. if the corresponding wave is a shock).

## 5. Summary of the Method.

The overall algorithm can be summarized in the pseudocode format as following:

```

 $t = 0$ 
Define initial conditions for  $[\rho, m, n, E, \phi]$ 
Compute  $u^0, v^0, p^0$ 
Initialize  $\phi^0$  and  $\rho^0$  using the interface sharpening procedure (Section 4.3)
Initialize  $U^0 = [\rho^0, m^0, n^0, E^0, \alpha^0, \beta^0]$  using  $\phi^0, \rho^0, u^0, v^0$ 
 $n = 0$ 
DO WHILE  $t < T_{end}$ 
     $t = t + \tau$ 
    Compute all the Jacobian matrices using  $U^n$  (see Appendix A)
    Compute all the artificial viscosity coefficients for the GP-dissipation term
    IF (reduction (Section 2.2) is on) THEN
         $U_0^{n+1} = U^n, \phi_0^{n+1} = \phi^n$ 
    ELSE
         $U_0^{n+1} = 0, \phi_0^{n+1} = 0$ 
    END IF
     $k = 0$ 
    DO WHILE ( $ER(U_k^{n+1}) > tolerance$ )
        Solve advection of the VoF function ((76) and (77)) for  $\phi_{k+1}^{n+1}$ 
        Solve (14) and (15) for  $U_{k+1}^{n+1}$ 
        Compute  $ER(U_{k+1}^{n+1})$ 
         $k = k + 1$ 
    END DO
    Compute  $u^{n+1}, v^{n+1}$ , and  $p^{n+1}$ 
    Use interface sharpening (Section 4.3) to update  $\rho^{n+1}$  and  $\phi^{n+1}$ 
    Update  $U^{n+1}$  using new values of  $\rho^{n+1}, \phi^{n+1}, u^{n+1}, v^{n+1}$ , and  $p^{n+1}$ 
     $n = n + 1$ 
END DO

```

## 6. Numerical Tests.

In this section, numerical tests are presented to verify the performance of the proposed method. Note, that no analytical or extensive numerical study on the stability region has been attempted. For each test, time step ( $\tau$ ) and space step ( $h$ ) are chosen to guarantee desired accuracy and stability, and the choice may not be optimal. Based on the performed tests, low Mach number applications do not impose significant stability restrictions, i.e. they at least allow the value of  $\tau$  to be several times higher than  $h$ . Stability regions in high Mach number applications depend on the types of the discontinuities in the flow, such as strengths of the shocks, but were found to be larger than ones for the explicit version of the method, for which CFL-condition is of the type  $\tau < const \cdot \frac{h}{|\lambda_{max}|}$  where  $|\lambda_{max}|$  is the maximum speed of propagation (see [4] for stability analysis of the explicit finite element Guermond-Popov scheme). Use of explicit non-reflection boundary conditions, as in Sections 6.8 and 6.9, is expected to strengthen the stability restrictions (e.g. see [44]).

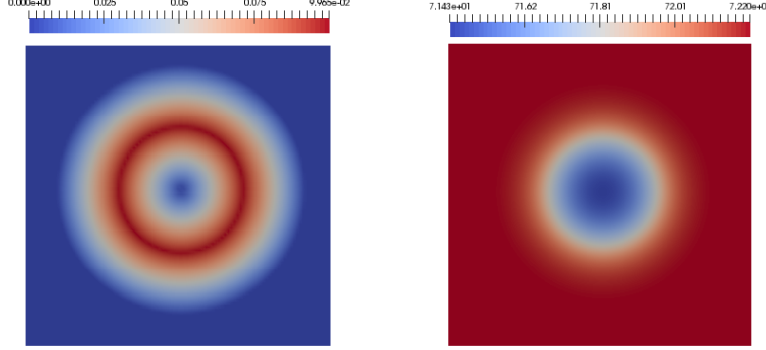


Figure 1: Initial Pressure and Mach number distributions for  $M_0 = 10^{-1}$ .

### 6.1. Gresho Vortex.

The behaviour of the scheme in the low Mach number limit is investigated using the Gresho vortex test (similar to [23]). It is a time-independent inviscid rotating vortex placed in a square periodic domain. Scaling of the pressure with respect to the reference Mach number allows studying the stability and dissipative properties of numerical methods for different Mach numbers (see [22] as an example).

Initial conditions are given by (see Figure 1 for initial pressure and Mach number distributions for  $M_0 = 10^{-1}$ )

$$p_0 = \frac{\rho_0}{\gamma M_0^2} \quad (109)$$

$$(u_\phi(r), p(r)) = \begin{cases} (5r, p_0 + \frac{25}{2}r^2), & \text{if } 0 \leq r < 0.2 \\ (2 - 5r, p_0 + \frac{25}{2}r^2 + 4(1 - 5r - \ln 0.2 + \ln 5)), & \text{if } 0.2 \leq r < 0.4 \\ (0, p_0 - 2 + 4 \ln 2), & \text{if } 0.4 \leq r \end{cases} \quad (110)$$

where  $M_0$  is the reference the Mach number,  $(r, \phi)$  - polar coordinates with origin in the center of the vortex.

The range of Mach numbers considered here is  $[10^{-6}; 10^{-1}]$ . As it can be seen in Figure 2, if no splitting error reduction technique is used the vortex is not well preserved in time and completely dissipated after one revolution (by the time  $t = 1$ ). However, if one step of the splitting error reduction, described in the Section 2.2, is used, the proper time-independent behavior is recovered (see Figure 3). The method remains efficient in the considered range of Mach numbers, i.e. choosing the reference Mach number as low

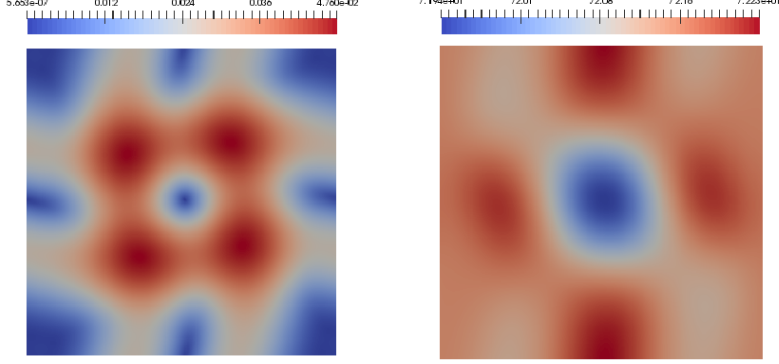


Figure 2: Pressure and Mach number distributions at  $t = 1$  for  $M_0 = 10^{-1}$ , no splitting error reduction.

as  $M_0 = 10^{-6}$  does not require any decrease of time or space steps. Figure 4 shows the time evolution of the relative kinetic energy for the computations described above. It can be concluded that the energy loss was due to the splitting error and its reduction allows one to recover conservative properties up to the influence of the artificial dissipation, required for stability.

All the tests are performed using the LM-dissipation term, described in Section 3.2. Parameters  $\omega_1$  and  $\omega_2$  are chosen for each  $M_0$  to guarantee acceptable rate of kinetic energy dissipation ( $\omega_1$ ) and dumping of high frequency oscillations ( $\omega_2$ ). Figures 6 and 8 illustrate the effect of these parameters. Figure 7 shows the ineffectiveness of the artificial dissipation operator of the type  $\mathbf{D}_1^{LM}U$  in dealing with node-to-node pressure oscillations, which have an increasing effect as  $M_0$  decreases. Figure 9 reveals that an increase of  $\omega_2$  alone leads to an increase of relative kinetic energy and consequently to a rise of instability, especially for relatively high Mach numbers such as  $M_0 = 10^{-1}$ . Therefore one needs to have both components of the LM-dissipation term. Such combination allows tuning the algorithm for a wide range of Mach numbers. Figure 5 shows that  $\frac{|p - p_{max}|}{p_{max}} \sim M^2$ , which is the proper scaling in the nearly incompressible regime (see [9] for details).

## 6.2. Sod Shock Tube.

The Sod Shock tube test (originally proposed in [45]) is used here to evaluate shock capturing properties of the method (when GP-dissipation term is used) and compare the implicit version of the scheme (IGP) with the explicit one (EGP), and with the classic Lax-Friedrichs method (LF).

The initial conditions are given by

$$\begin{bmatrix} \rho_L \\ p_L \\ u_L \end{bmatrix} = \begin{bmatrix} 1.0 \\ 1.0 \\ 0.0 \end{bmatrix} \quad (111)$$

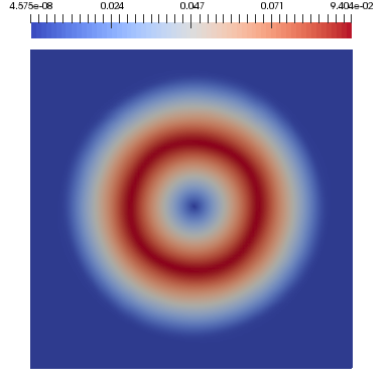


Figure 3.a:  $M_0 = 10^{-1}$

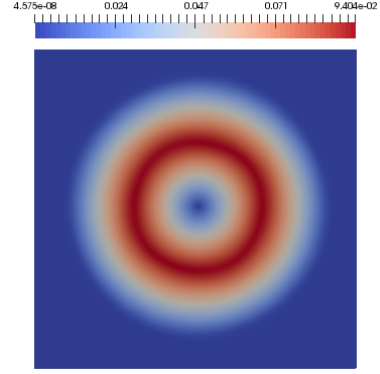


Figure 3.b:  $M_0 = 10^{-2}$

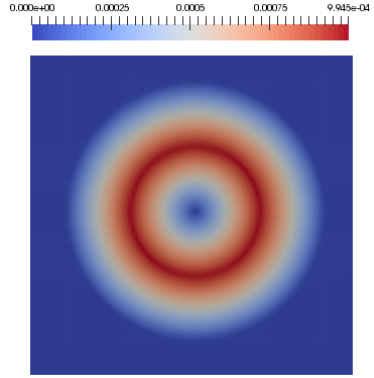


Figure 3.c:  $M_0 = 10^{-3}$

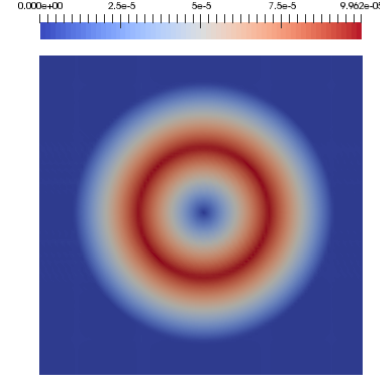


Figure 3.d:  $M_0 = 10^{-4}$

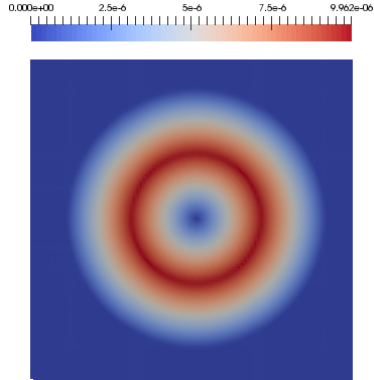


Figure 3.e:  $M_0 = 10^{-5}$

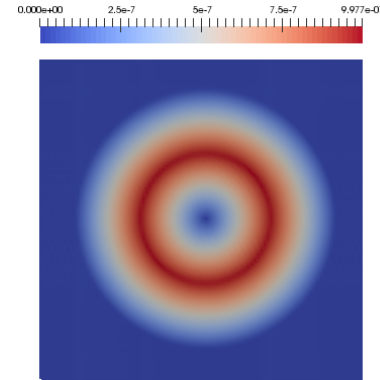


Figure 3.f:  $M_0 = 10^{-6}$

Figure 3: Mach number distributions at  $t=1$  for different  $M_0$  computed using the splitting error reduction technique. In all the tests  $\tau = 10^{-3}$ , grid size:  $100 \times 100$ .

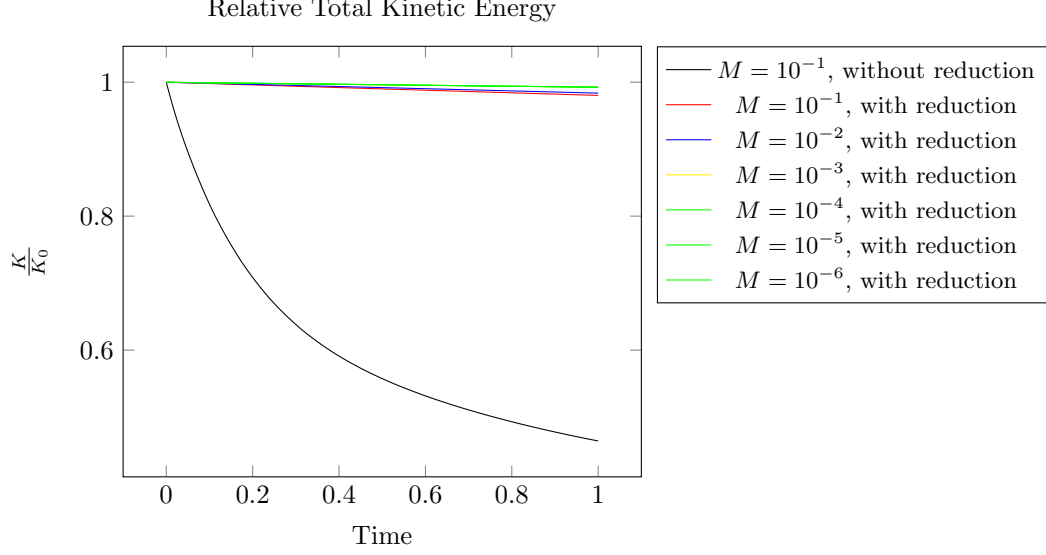


Figure 4: Time evolution of the Relative Kinetic Energy for different test cases. In all the tests  $\tau = 10^{-3}$ , grid size: 100x100.

$$\begin{bmatrix} \rho_R \\ p_R \\ u_R \end{bmatrix} = \begin{bmatrix} 0.125 \\ 0.1 \\ 0.0 \end{bmatrix} \quad (112)$$

The results at  $T_{end} = 0.1$  for the density ( $\rho$ ), pressure ( $p$ ), velocity ( $u$ ) and internal energy ( $e$ ) are presented in Figure 10 ( $h = 10^{-3}$ ) and Figure 11 ( $h = 0.5 \cdot 10^{-3}$ ). In both cases  $\tau = 10^{-4}$ .

It can be seen that explicit and implicit versions of the Guermond-Popov scheme produce almost equivalent solutions in both cases. On a coarser grid, when space error term has a dominant contribution to the overall error, the Guermond-Popov scheme maintains significantly sharper profiles of discontinuities in the solution than the Lax-Friedrichs method.

### 6.3. Taylor-Green Vortex.

The Taylor-Green vortex is a well-known exact solution for incompressible NSEs (see e.g. [46],[47]). It was also used for verification of compressible solvers at low Mach numbers (see e.g. [20], [48]). Here it is used to demonstrate the ability of the algorithm to simulate effects of viscosity and approximate solutions of the incompressible NSEs.

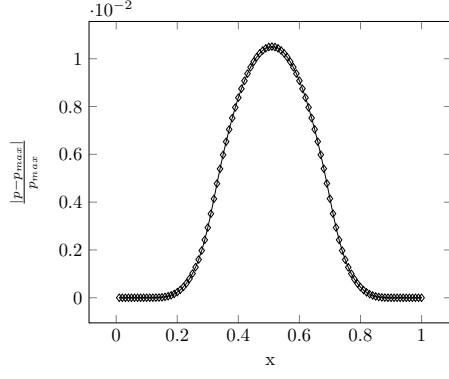


Figure 5.a:  $M_0 = 10^{-1}$

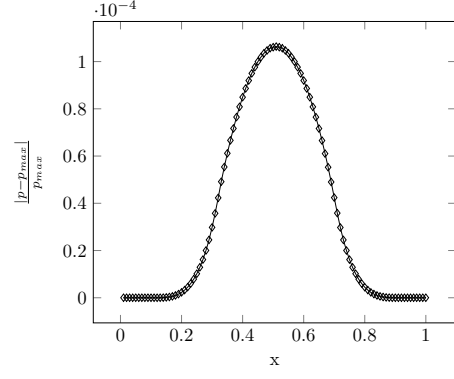


Figure 5.b:  $M_0 = 10^{-2}$

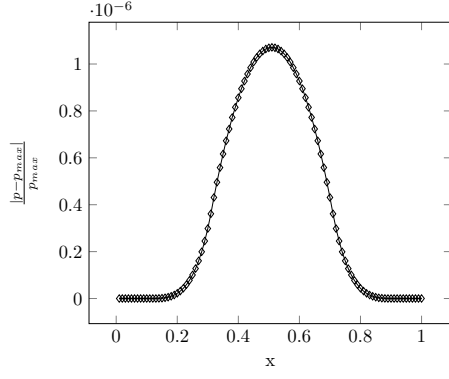


Figure 5.c:  $M_0 = 10^{-3}$

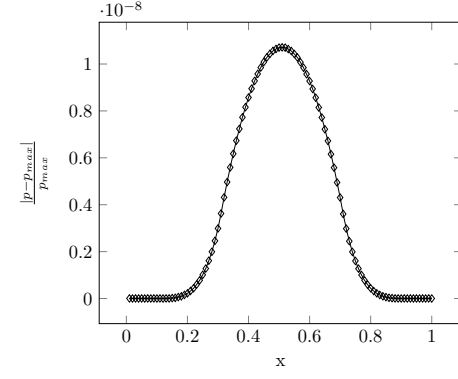


Figure 5.d:  $M_0 = 10^{-4}$

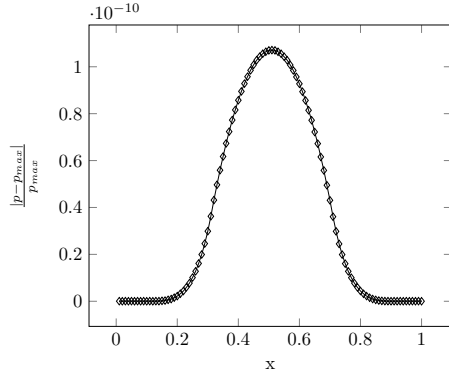


Figure 5.e:  $M_0 = 10^{-5}$

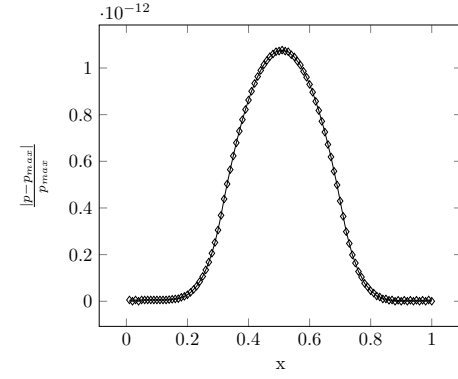


Figure 5.f:  $M_0 = 10^{-6}$

Figure 5: Relative pressure variations for different  $M_0$ , cross-sections at  $x = 0.5$ . In all the tests  $\tau = 10^{-3}$ , grid size: 100x100.



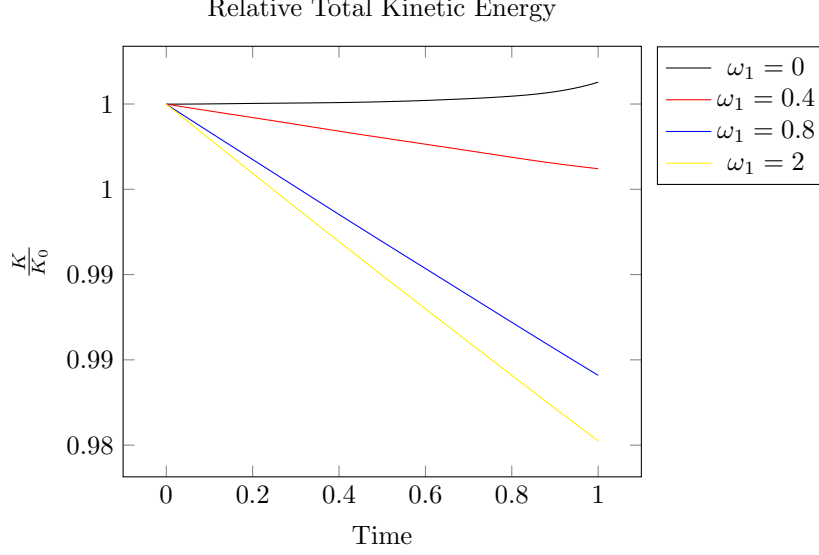


Figure 6: Time evolution of the Relative Kinetic Energy depending on the value of  $\omega_1$ . In all the tests  $\omega_2 = 0$ ,  $M_0 = 10^{-1}$ ,  $\tau = 10^{-3}$ , grid size: 100x100.

The exact solution on a periodic  $[0, 2\pi] \times [0, 2\pi]$  domain is given by

$$\rho = 1 \quad (113)$$

$$u = u_0 \cos x \sin y \exp^{-2 \frac{\mu t}{\rho}} \quad (114)$$

$$v = u_0 \sin x \cos y \exp^{-2 \frac{\mu t}{\rho}} \quad (115)$$

$$p = p_0 - \frac{\rho u_0^2}{4} (\cos 2x + \cos 2y) \exp^{-4 \frac{\mu t}{\rho}}. \quad (116)$$

Here  $M_0 = \frac{u_0}{\sqrt{\frac{\gamma p_0}{\rho}}} \sim \frac{u_0}{\sqrt{p_0}}$ . Defining  $p_0 = 1$ ,  $\gamma = 1.4$ ,  $M_0$  can be varied by changing  $u_0$ , as it was proposed in [48]. Hence  $M_0 \sim u_0$ . For this test, a single-step version of the splitting error reduction procedure was used.

Figure 12 represents the time evolution of Relative Kinetic Energy for different values of  $\mu$  ( $M = 10^{-6}$ ). The results show good agreement with the analytical solution for the incompressible case. As it can be seen from Figure 13, change of the Mach number from  $M = 10^{-6}$  to  $M = 10^{-1}$  does not change the behavior of Relative Kinetic Energy, which remains in a good agreement with the incompressible theory. Figure 14 shows the behavior of the discrete  $L_\infty$  norm of the pressure error under temporal and spatial grid refinement for different values of the Mach number. Similar results were obtained for  $u$  and  $v$ .

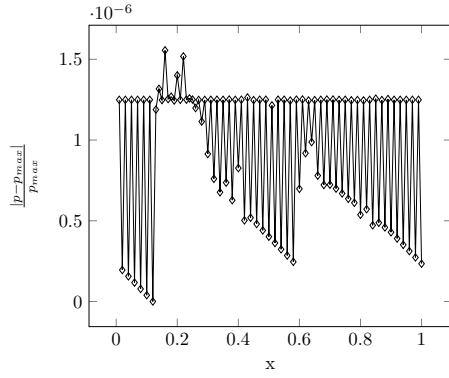


Figure 7.a:  $\omega_1 = 0$

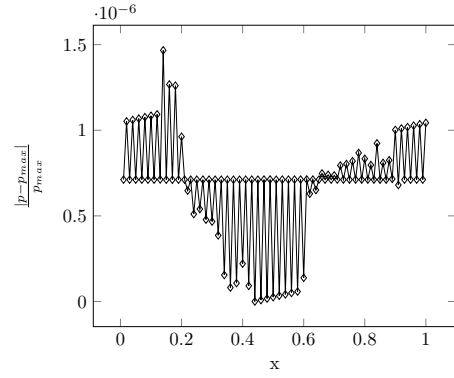


Figure 7.b:  $\omega_1 = 0.4$

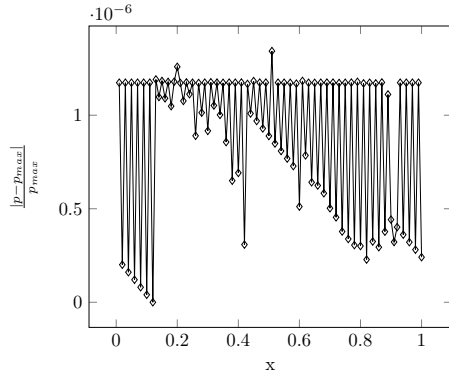


Figure 7.c:  $\omega_1 = 0.8$

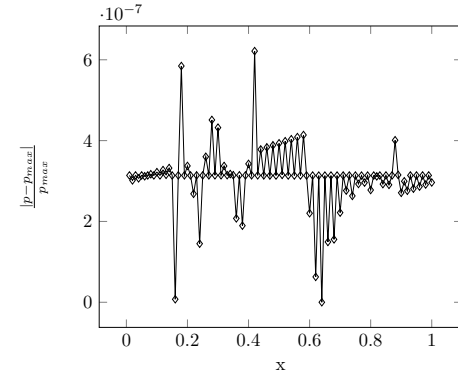


Figure 7.d:  $\omega_1 = 1$

Figure 7: Relative pressure variation after one time step, cross-section at  $x = 0.5$ , for different values of  $\omega_1$ . Further integration leads to a numerical failure. In all the tests  $\omega_2 = 0$ ,  $M_0 = 10^{-6}$ ,  $\tau = 10^{-3}$ , grid size: 100x100.

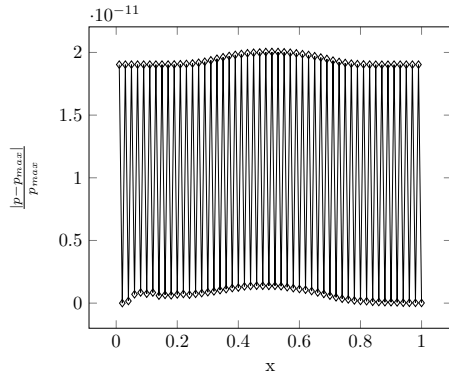


Figure 8.a:  $\omega_2 = 0.01$

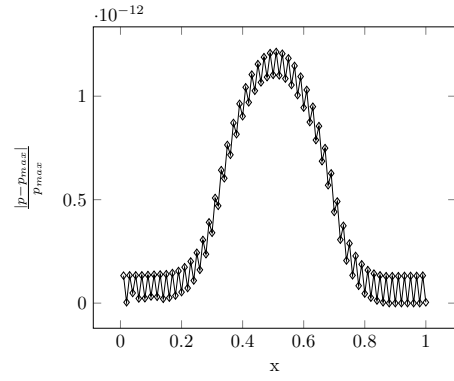


Figure 8.b:  $\omega_2 = 0.1$

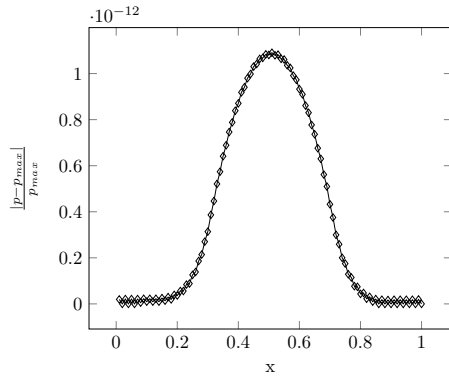


Figure 8.c:  $\omega_2 = 0.5$

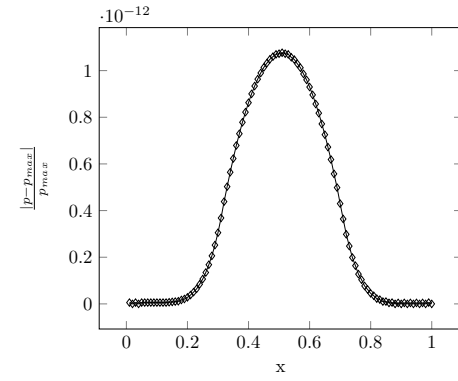


Figure 8.d:  $\omega_2 = 1.1$

Figure 8: Relative pressure variations after one time step, cross-section at  $x = 0.5$ , for different values of  $\omega_2$ . In all the tests  $\omega_1 = 1$ ,  $M_0 = 10^{-6}$ ,  $\tau = 10^{-3}$ , grid size: 100x100.

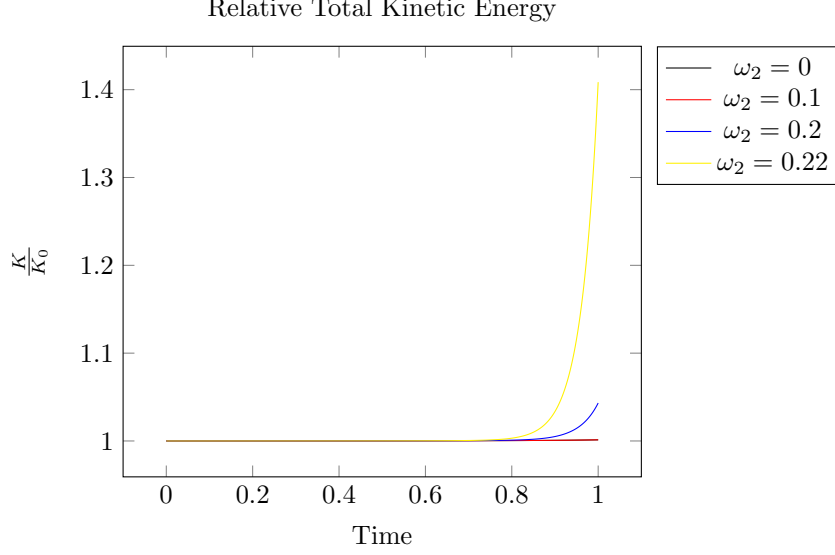


Figure 9: Time evolution of the Relative Kinetic Energy depending on the value of  $\omega_2$ . In all the tests  $\omega_1 = 0$ ,  $M_0 = 10^{-1}$ ,  $\tau = 10^{-3}$ , grid size: 100x100.

#### 6.4. One Dimensional Interface Advection.

Here an advection of an interface between air ( $\gamma = 1.4$ ,  $\pi^\infty = 0$ ) and water ( $\gamma = 6.12$ , non-dimensiolized  $\pi^\infty = 0.1631$ ) under the atmospheric pressure is considered (similar to [20]). The purpose of the test is to demonstrate the absence of spurious pressure oscillations and preservation of pressure and velocity equilibrium for the method with both GP and LM ( $\omega_1 = 10$ ,  $\omega_2 = 1$ ) dissipation terms.

Initial conditions are given by

$$(\rho, u, p, \phi) = \begin{cases} (1, 0.1, 4.819 \times 10^{-5}, 1), & \text{if } x \leq 0.3 \\ (1.204 \times 10^{-3}, 0.1, 4.819 \times 10^{-5}, 0), & \text{if } x > 0.3 \end{cases} \quad (117)$$

and regularized after that by performing interface sharpening procedure until convergence. It is evolved with  $\tau = 10^{-2}$  on a uniform grid of 130 cells till  $t_{end} = 4$ . The results and initial conditions are shown in Figure 10.

In both cases (LM- and GP-dissipation terms) contact discontinuity is well preserved and no spurious oscillations are introduced, despite the high density ratio. Sharp profile of the interface is well maintained.

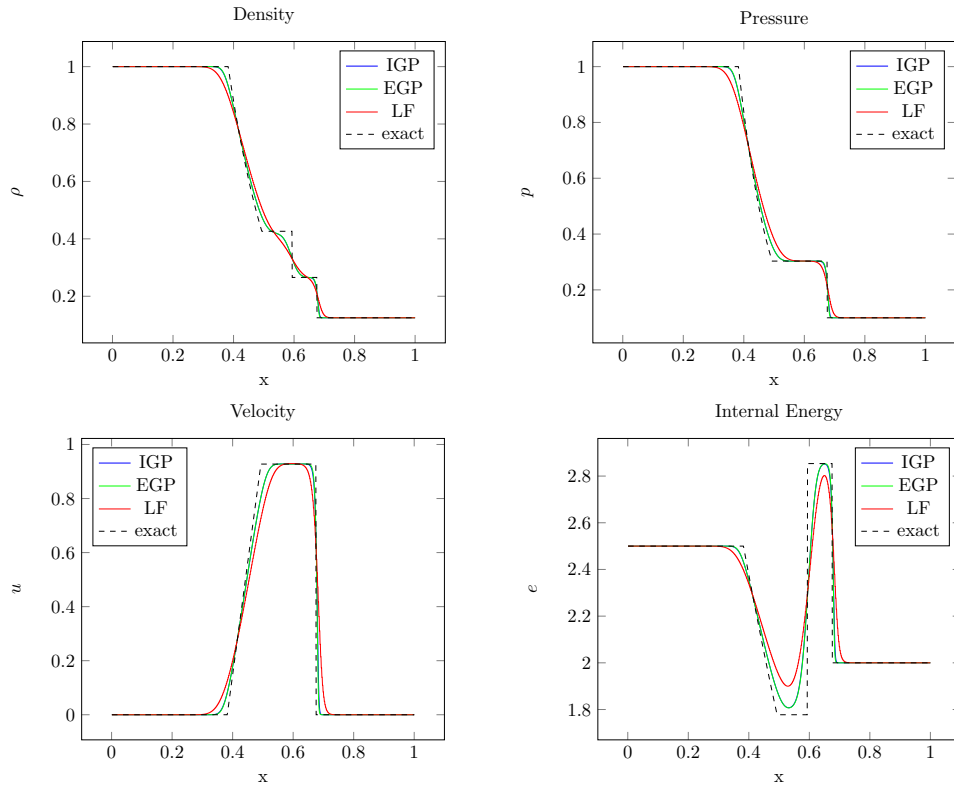


Figure 10: Sod Shock Tube test,  $T_{end} = 10^{-1}$ ,  $h = 10^{-3}$

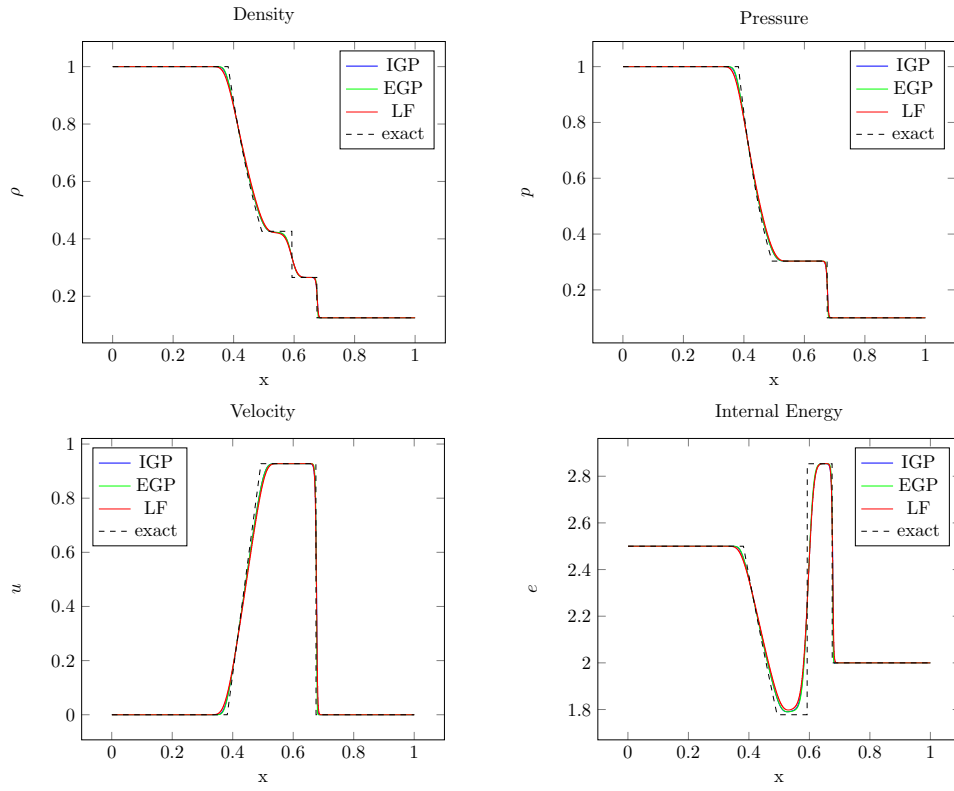


Figure 11: Sod Shock Tube test,  $T_{end} = 10^{-1}$ ,  $h = 0.5 \cdot 10^{-3}$

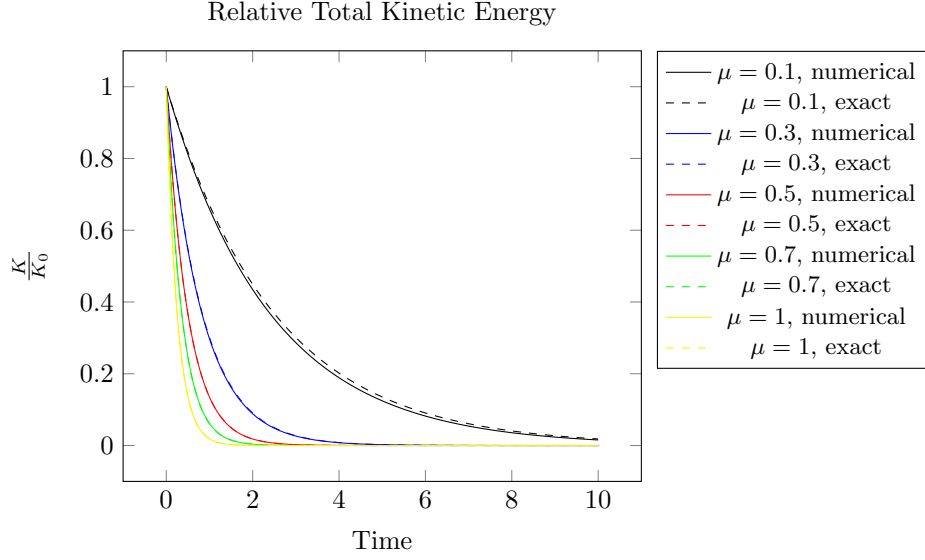


Figure 12: Time evolution of Relative Total Kinetic Energy for different values of viscosity.  $M \sim 10^{-6}$ ,  $\tau = 10^2$ ,  $h = 6.28 \cdot 10^{-2}$ .

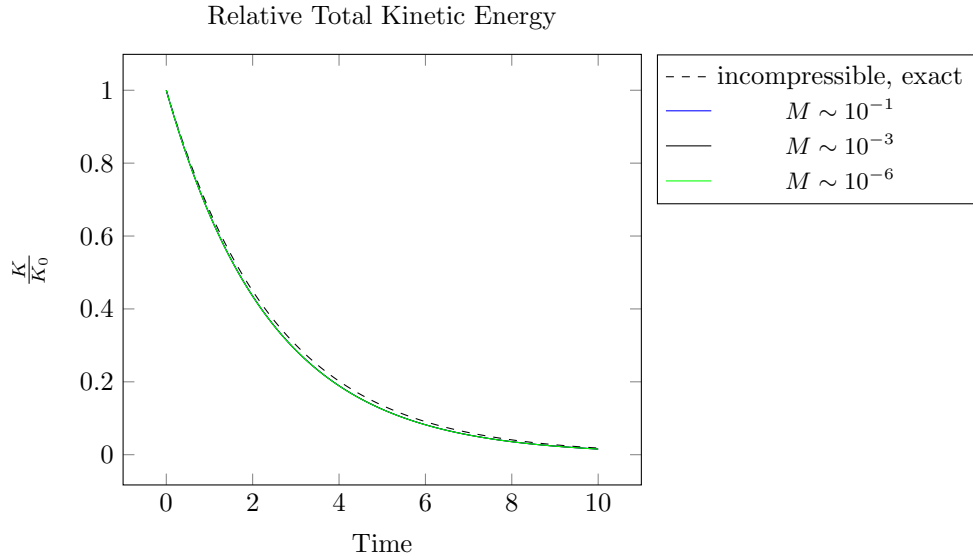


Figure 13: Time evolution of Relative Total Kinetic Energy for different values of the Mach number.  $\mu = 0.1$ ,  $\tau = 10^{-2}$ ,  $h = 6.28 \cdot 10^{-2}$ .

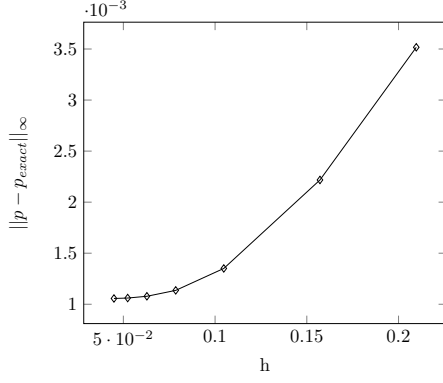


Figure 14.a:  $\tau = 10^{-3}$ ,  $M \sim 10^{-1}$

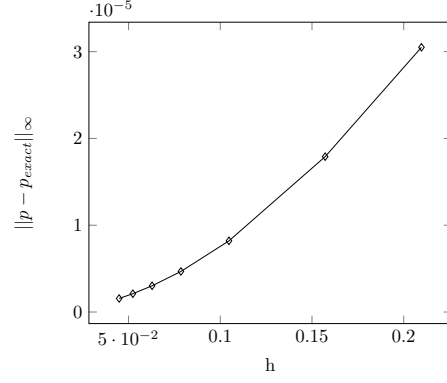


Figure 14.b:  $\tau = 10^{-3}$ ,  $M \sim 10^{-3}$

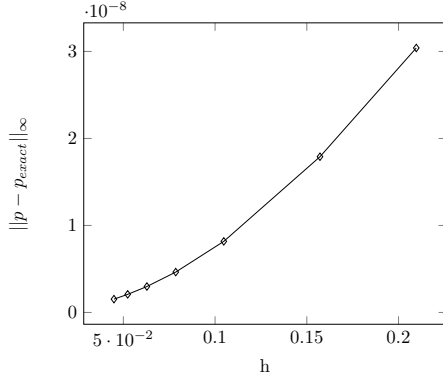


Figure 14.c:  $\tau = 10^{-3}$ ,  $M \sim 10^{-6}$

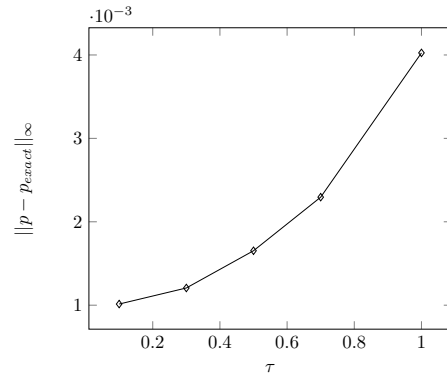


Figure 14.d:  $h = 1.85 \cdot 10^{-2}$ ,  $M \sim 10^{-1}$

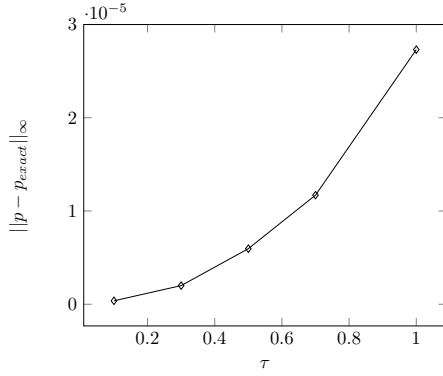


Figure 14.e:  $h = 1.85 \cdot 10^{-2}$ ,  $M \sim 10^{-3}$

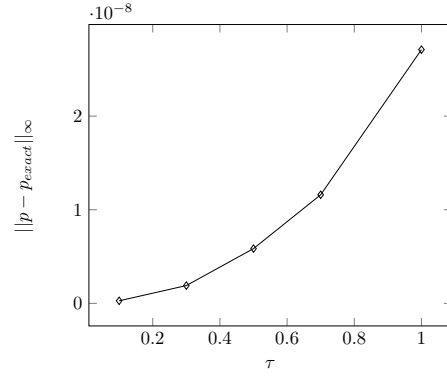


Figure 14.f:  $h = 1.85 \cdot 10^{-2}$ ,  $M \sim 10^{-6}$

Figure 14: Discrete  $L_{\infty}$  norm of the pressure error for different values of  $\tau$ ,  $M$ , and  $h_x = h_y = h$ .



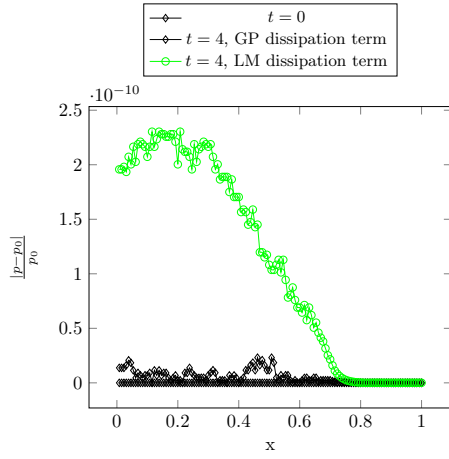


Figure 15.a: Relative Pressure Error

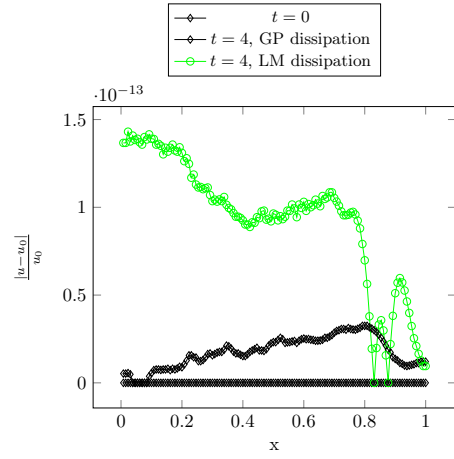


Figure 15.b: Relative Velocity Error

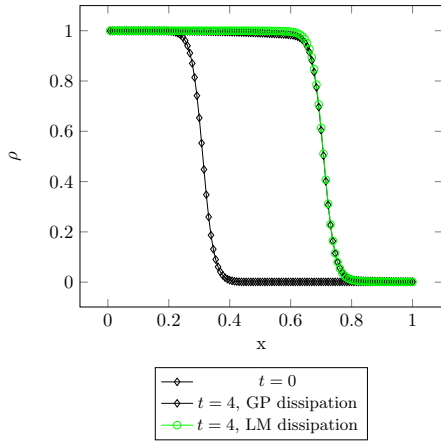


Figure 15.c: Density

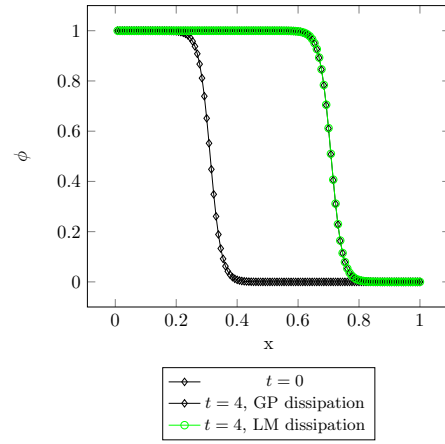


Figure 15.d: VoF-function

Figure 15: Interface advection using GP and LM artificial dissipation terms

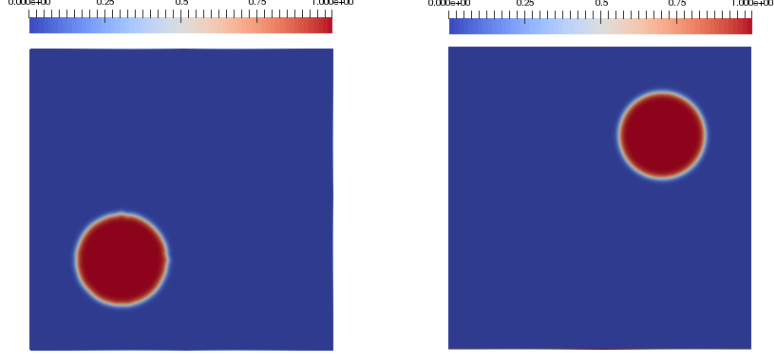


Figure 16: VoF-function at  $t = 0$  (left) and  $t = 4$  (right)

### 6.5. Two-Dimensional Interface Advection.

Here a water drop of the radius 0.15 is considered. It is located in the lower left angle of a square  $1 \times 1$  domain at  $(0.3, 0.3)$  at the initial moment of time and surrounded by air (both water and air have the same parameters as in the previous test). The bubble is then advected to the upper right angle of the domain,  $u = v = 0.1$ . The problem is discretized with  $\tau = 10^{-2}$  on a  $200 \times 200$  uniform grid. No splitting error reduction was performed for this test. LM dissipation is used ( $\omega_1 = 10$ ,  $\omega_2 = 0$ ).

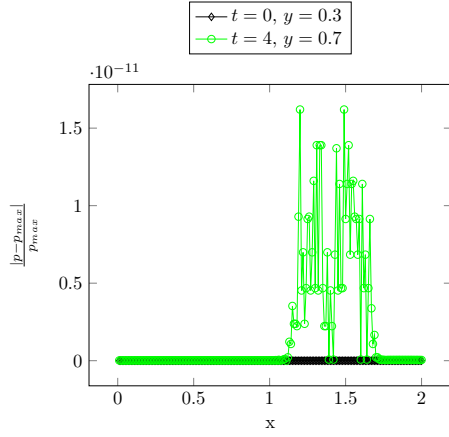


Figure 17.a: Pressure

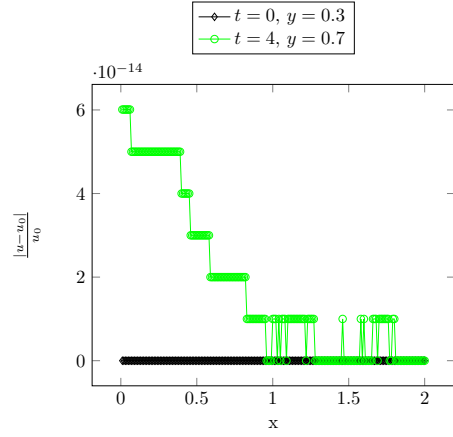


Figure 17.b: Velocity

Figure 17: Relative Pressure and Velocity Errors, cross-sections at  $y = 0.3$  and  $y = 0.7$

As can be seen in figures 16 and 17 the shape of the bubble is well preserved, no spurious oscillations or artificial acoustic waves are introduced.

$\epsilon$	$E(\Delta p)$	$\ u\ _\infty$
0.5	0.0755	$1.79 \cdot 10^{-5}$
1	0.0793	$4.1 \cdot 10^{-4}$
1.5	0.1149	$2.4 \cdot 10^{-4}$

Table 1:  $E(\Delta p)$  and  $\|u\|_\infty$  for different values of  $\epsilon$  (i.e. for different interface thickness).

#### 6.6. Laplace formula.

Following [6] and [41], the implementation of surface tension is verified by reproducing pressure jump across a curved interface, given by the Laplace formula. In case of the cylindrical interface:

$$\Delta p_{exact} = \sigma/R \quad (118)$$

where  $R$  is the radius of the cylinder.

At the initial moment of time, a liquid ( $\rho_l, \gamma = 2.4, \pi^\infty = 10^7 \text{ Pa}$ ) cylindrical drop of radius  $R = 0.3 \text{ m}$  centered at  $(0.5 \text{ m}, 0.5 \text{ m})$  is placed in a  $1 \text{ m} \times 1 \text{ m}$  square domain with symmetry boundary conditions, surrounded by gas ( $\rho_g = 1 \text{ kg/m}^3, \gamma = 1.4, \pi^\infty = 0 \text{ Pa}$ ). Pressure is given by the Laplace formula, with pressure outside of the drop  $p_{out} = 100 \text{ Pa}$ , and inside  $p_{in} = p_{out} + \Delta p_{exact}$ .

Relative pressure jump error ( $E(\Delta p) = \frac{\Delta p - \Delta p_{exact}}{\Delta p_{exact}}$ ), and numerical  $R$  is computed by an averaging procedure, similar to the one in [6]. Nodes with  $\phi \geq 0.9$  are considered to be inside, and nodes with  $\phi < 0.9$  to be outside of the drop. As in [41], spatial convergence of the method is evaluated by measuring the  $E(\Delta p)$  after one time step for different grid sizes. No splitting error reduction was performed for this test. Results are shown in Figure 18.a.

Figure 18.b shows the increase of the discrete  $L_\infty$  (maximum) norm of the velocity (i.e. increase of magnitude of parasitic current) under grid refinement. Similar effect was described in [41] for some other implementations of CSF approach. No quantitative results on parasitic currents for the method were presented in the original paper [6] to compare with, thus their influence on accuracy and stability of the method remains an open question. Figures 19-20 demonstrate the dependence of pressure and velocity errors after one time step on values of  $\sigma$  and  $\rho_l$ . Longtime evolution of the  $E(\Delta p)$  for  $\rho_l = 10 \text{ kg/m}^3, \sigma = 1 \text{ N/m}$ , and different values of  $h_x = h_y = h$  is shown in Figure 21. The thickness of the interface is also expected to play a role in the accuracy of the approximation. As it is shown in Table 1, thinner interface (smaller value of  $\epsilon$ ) leads to a smaller error in the pressure jump.

For all values of the parameters considered above, errors remain small. The method is shown to be convergent in space in terms of the pressure error, thus the Laplace law is reproduced by the algorithm. Further investigation of parasitic currents and influence of various parameters of the problem, as well as an amount of artificial dissipation, on long-time accuracy and stability of the method is an interesting perspective.

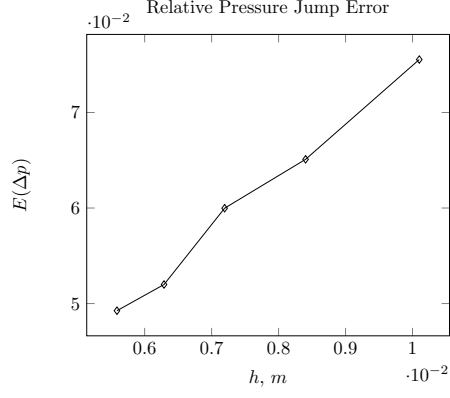


Figure 18.a

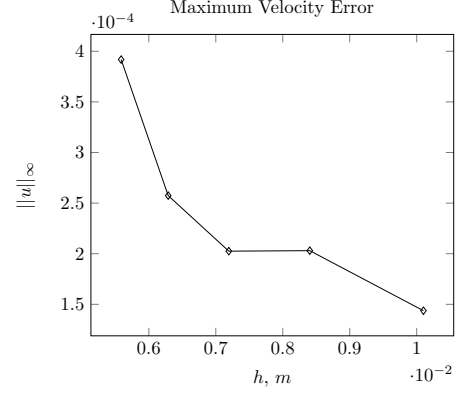


Figure 18.b

Figure 18:  $E(\Delta p)$  and  $\|u\|_{\infty}$  after one time step on different grids.  $\sigma = 1 \text{ N/m}$ ,  $\rho_l = 100 \text{ kg/m}^3$ ,  $\tau = 10^{-5} \text{ s}$ .

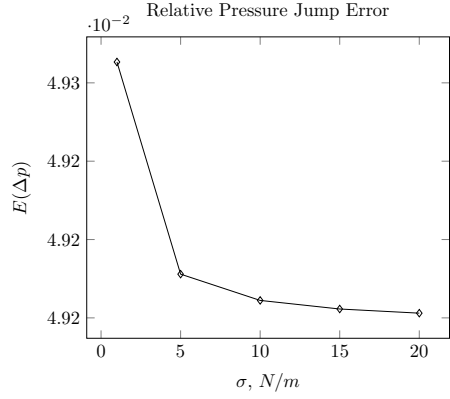


Figure 19.a

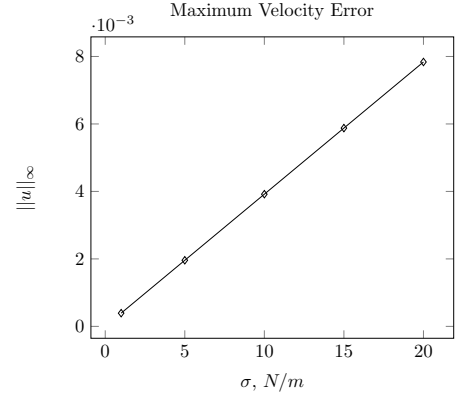


Figure 19.b

Figure 19:  $E(\Delta p)$  and  $\|u\|_{\infty}$  after one time step for different  $\sigma$ .  $h = 5.6 \cdot 10^{-3} \text{ m}$ ,  $\rho_l = 100 \text{ kg/m}^3$ ,  $\tau = 10^{-5} \text{ s}$ .

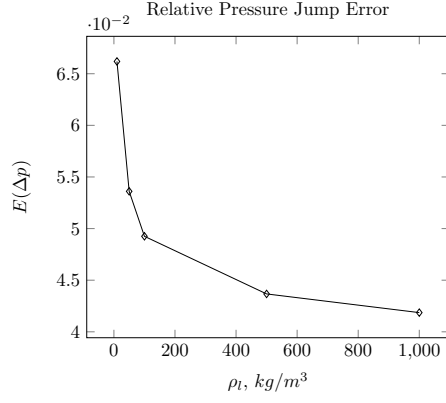


Figure 20.a

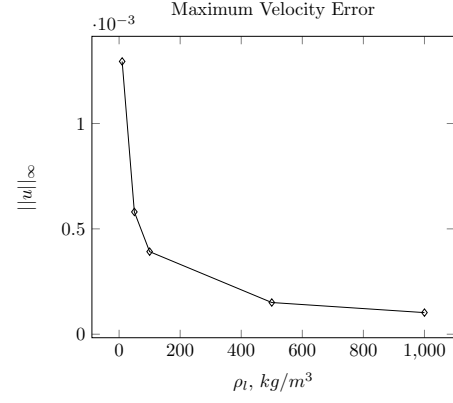


Figure 20.b

Figure 20:  $E(\Delta p)$  and  $\|u\|_\infty$  after one time step for different  $\rho_l$ .  $h = 5.6 \cdot 10^{-3} \text{ m}$ ,  $\sigma = 1 \text{ N/m}$ ,  $\tau = 10^{-5} \text{ s}$ .

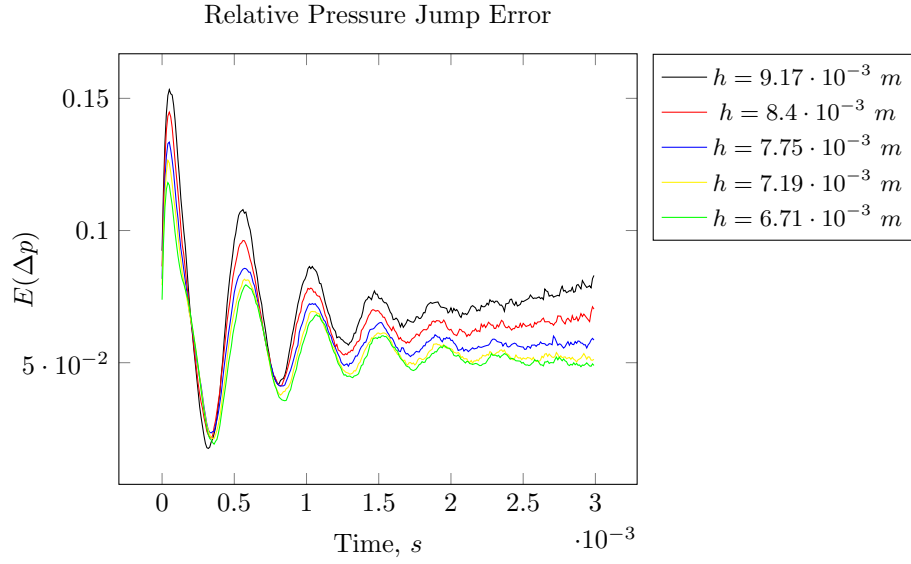


Figure 21: Time evolution of the Relative Pressure Jump Error with different grid sizes. In all the tests  $\tau = 10^{-5} \text{ s}$ ,  $\sigma = 1 \text{ N/m}$ ,  $\rho_l = 10 \text{ kg/m}^3$ .

### 6.7. One Dimensional Shock Wave-Interface Interaction.

Next, a one dimensional shock-interface interaction is studied using a test case from [31] and [20]. A strong, Mach 8.96, shockwave is travelling in helium ( $\gamma = 1.667$ ,  $\pi^\infty = 0$ ) towards a material with air ( $\gamma = 1.4$ ,  $\pi^\infty = 0$ ). Both materials are assumed to be inviscid. Following [49], non-dimensional initial conditions are given by

$$(\rho, u, p, \phi) = \begin{cases} (0.386, 26.59, 100, 1) & \text{if } 0 \leq x < 0.2 \\ (0.1, -0.5, 1, 1) & \text{if } 0.2 \leq x < 0.8 \\ (1, -0.5, 1, 0) & \text{if } 0.8 \leq x < 2 \end{cases} \quad (119)$$

Such problems are known to be challenging, since interface sharpening methods often lead to miscomputations of shock positions and speed (see [20]). Here, a numerical solution at  $T_{end} = 0.07$  ( $\tau = 1 \cdot 10^{-5}$ ,  $h = 10^{-3}$ ) is compared with the exact one (derived in [31]). GP-dissipation term is used to stabilize the solution. The interface sharpening procedure is used with the parameter  $\epsilon = 0.5$ . The results are present in Figure 22.

As it can be seen, the interface remains very sharp, although density appears to be smeared in the regions adjacent to the artificial mixing layer. Shock positions and strengths are computed correctly and no oscillations are present. Thus, the method can be used to compute shock-interface interaction problems.

### 6.8. Shock Wave Refraction.

Following [50], two dimensional shock-interface interaction is studied using Euler equations (no surface tension, viscous and heat transfer effects). In a square  $1m \times 1m$  domain, a normal incident shock wave is propagating to the left in water ( $\gamma = 4.4$ ,  $\pi_\infty = 6 \cdot 10^8 \text{ Pa}$ ) and impacting a planar material interface with air ( $\gamma = 1.4$ ), inclined on an angle  $\beta$ .

The following pre- and post-shock conditions are specified for water in term of primitive variables  $(p, \rho, u, v)$  in  $(Pa, kg/m^3, m/s, m/s)$  (similar to [50]):

$$(p, \rho, u, v)_{pre} = (1 \cdot 10^5, 1000, 0, 0) \quad (120)$$

$$(p, \rho, u, v)_{post} = (1.9 \cdot 10^9, 1323.65, -681.58, 0) \quad (121)$$

and the initial state of air is specified as:

$$(p, \rho, u, v)_{air} = (1 \cdot 10^5, 1, 0, 0). \quad (122)$$

Initial fields of  $\rho$  for angles  $\beta = \frac{\pi}{6}, \frac{\pi}{4.5}, \frac{\pi}{3.6}, \frac{\pi}{2.5}$  are shown in Figure 23.

Non-reflection boundary conditions (proposed in [51]) are prescribed explicitly at the left, right, and top boundaries of the domain, symmetry boundary conditions are used at the bottom. The computations are performed on a  $800 \times 800$  uniform grid, with  $\tau = 10^{-7}$  s. No splitting error reduction was performed for this test.

Figures 24-27 represent  $\log p$ ,  $\phi$ , and  $\rho$  at  $T_{end} = 1.5 \cdot 10^{-4}$  s. The results are in a good agreement with those from [50]. The material interface remains thin throughout the computations ( $\epsilon = 1$ ), correct refraction patterns are captured. Cases of  $\beta = \frac{\pi}{6}, \frac{\pi}{4.5}, \frac{\pi}{3.6}$  produce regular refraction pattern with reflected expansion (RRE), while the case of

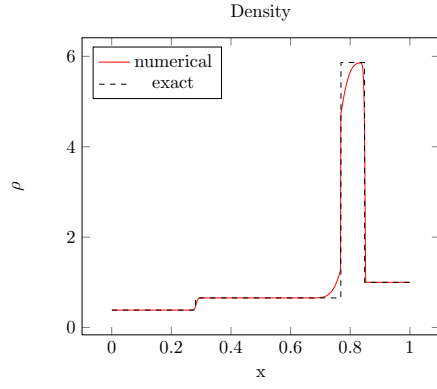


Figure 22.a

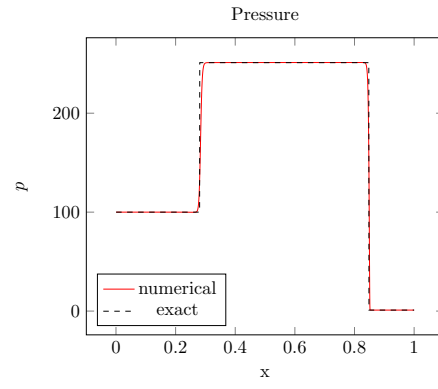


Figure 22.b

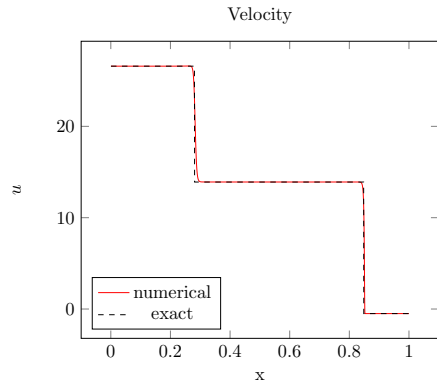


Figure 22.c

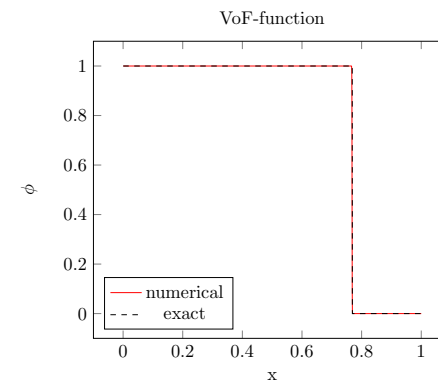


Figure 22.d

Figure 22: Density, pressure, velocity and VoF-function at  $T_{end} = 0.07$ . Exact and numerical ( $\tau = 1 \cdot 10^{-5}$ ,  $h = 10^{-3}$ ) solutions.

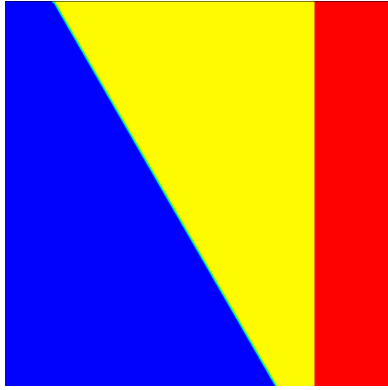


Figure 23.a:  $\beta = \frac{\pi}{6}$

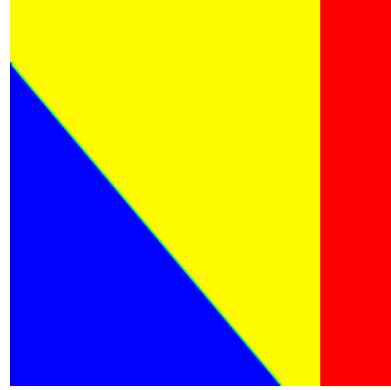


Figure 23.b:  $\beta = \frac{\pi}{4.5}$

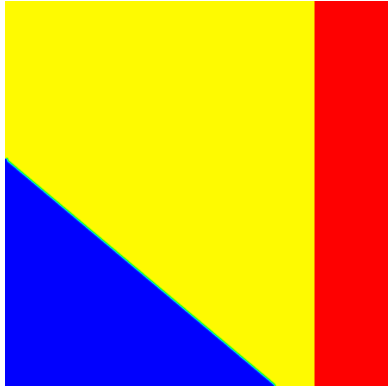


Figure 23.c:  $\beta = \frac{\pi}{3.6}$

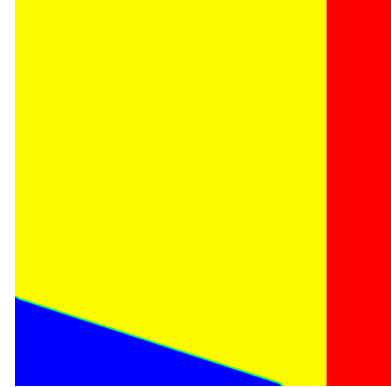


Figure 23.d:  $\beta = \frac{\pi}{2.5}$

Figure 23: Initial  $\rho$ -fields (pseudocolor) for different values of  $\beta$ . Red - water post-shock state, yellow - water pre-shock state, blue - air.



$\beta = \frac{\pi}{2.5}$  gives rise to the irregular concave forward refraction (CFR), as impacted wave interacts with the reflected expansion, “which results in a mutual annihilation and formation of a compound wave” (see [50]). The compound wave is curved due to the speed difference between the incident shock and the refraction node (intersection of the compound and transmitted waves), and weaker than the impacting shock. In all the test cases a water jet is being formed by the convergence of shock-induced flows, which is also in agreement with the results of [50].

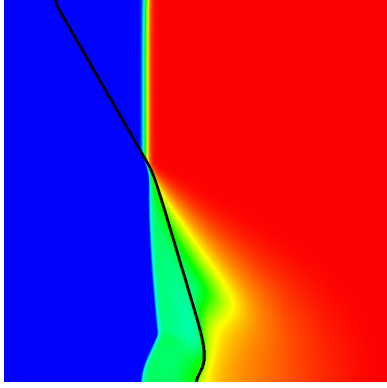


Figure 24.a:  $\log p$  and  $\phi$

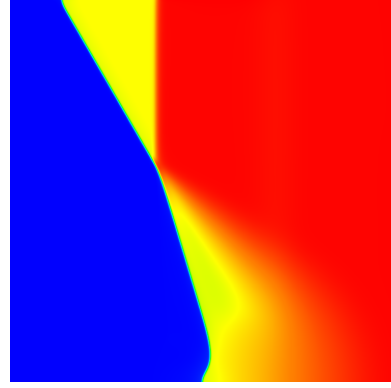


Figure 24.b:  $\rho$

Figure 24:  $\log p$  (pseudocolor),  $\phi$  (contour), and  $\rho$  (pseudocolor) plots at  $T_{end} = 1.5 \cdot 10^{-4}$  s for  $\beta = \frac{\pi}{6}$

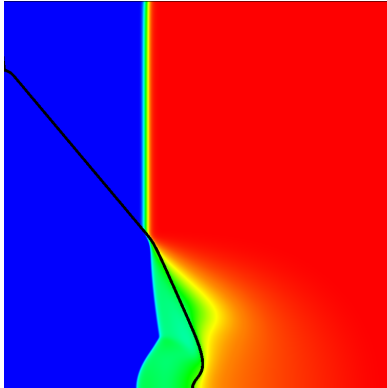


Figure 25.a:  $\log p$  and  $\phi$

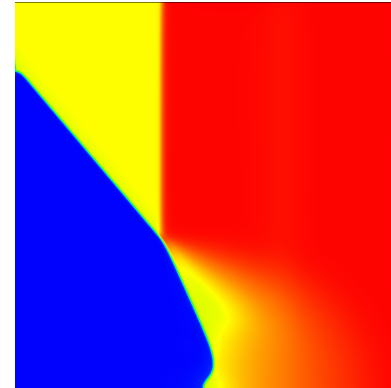


Figure 25.b:  $\rho$

Figure 25:  $\log p$  (pseudocolor),  $\phi$  (contour), and  $\rho$  (pseudocolor) plots at  $T_{end} = 1.5 \cdot 10^{-4}$  s for  $\beta = \frac{\pi}{4.5}$

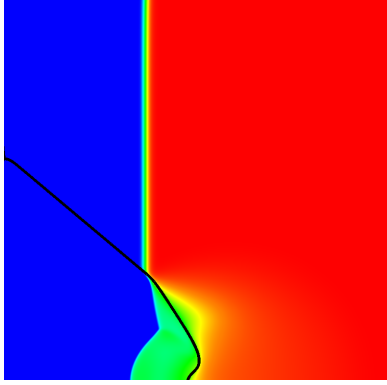


Figure 26.a:  $\log p$  and  $\phi$

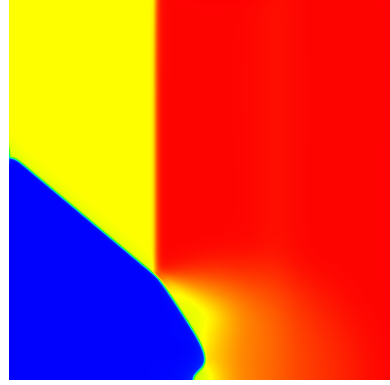


Figure 26.b:  $\rho$

Figure 26:  $\log p$  (pseudocolor),  $\phi$  (contour), and  $\rho$  (pseudocolor) plots at  $T_{end} = 1.5 \cdot 10^{-4}$  s for  $\beta = \frac{\pi}{3.6}$

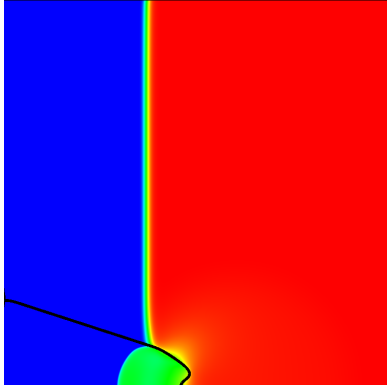


Figure 27.a:  $\log p$  and  $\phi$

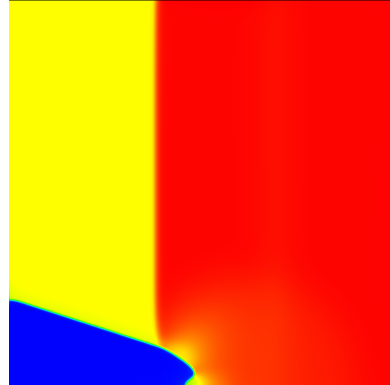


Figure 27.b:  $\rho$

Figure 27:  $\log p$  (pseudocolor),  $\phi$  (contour), and  $\rho$  (pseudocolor) plots at  $T_{end} = 1.5 \cdot 10^{-4}$  s for  $\beta = \frac{\pi}{2.5}$

### 6.9. Shock Wave-Bubble Interaction.

In this test the same materials and the same initial conditions (pre-,post-shock state, location of the shock wave) are used as in the previous test, but the interface forms an air bubble of the radius  $R = 0.2m$  centered at  $(0.55m, 0.5m)$ . The full system of NSEs is considered here, with  $\mu_{water} = 10^{-3} \text{ kg}/(s \cdot m)$ ,  $\mu_{air} = 10^{-5} \text{ kg}/(s \cdot m)$ ,  $\sigma = 0.073 \text{ N}/m$ . Interface sharpening is performed with the value of parameter  $\epsilon = 1.5$ . Initial conditions for air are given by:

$$(p, \rho, u, v)_{air} = (1 \cdot 10^5 + \frac{\sigma}{R}, 1, 0, 0). \quad (123)$$

The computation are performed on a  $800 \times 800$  uniform grid, with  $\tau = 10^{-7} \text{ s}$ . No splitting error reduction was performed for this test.  $\rho$  and  $\phi$  fields at different times are presented in Figures 28-34. The results are in a good agreement with [25], where a similar test case was presented. The interface remains thin throughout the computations, effects of wave refraction and eventual topological change (bubble collapse) with a formation of a high-speed jet are well-captured.

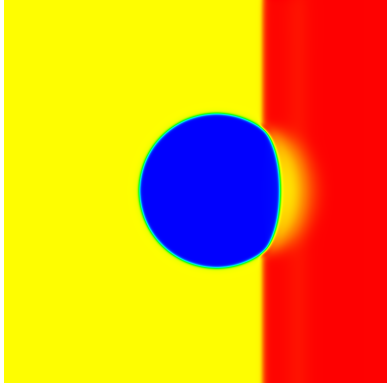


Figure 28.a:  $\rho$

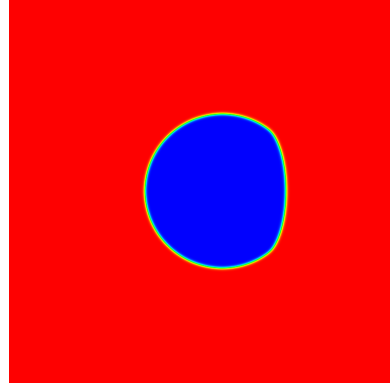


Figure 28.b:  $\phi$

Figure 28:  $\rho$  and  $\phi$  pseudocolor fields at  $t = 4.5 \cdot 10^{-5} \text{ s}$

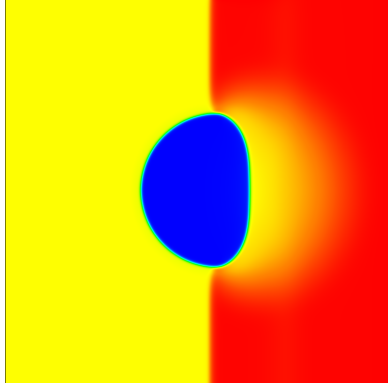


Figure 29.a:  $\rho$

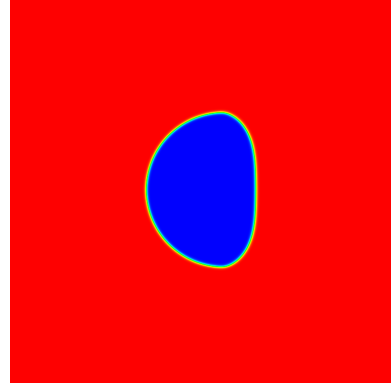


Figure 29.b:  $\phi$

Figure 29:  $\rho$  and  $\phi$  pseudocolor fields at  $t = 9.5 \cdot 10^{-5} \text{ s}$

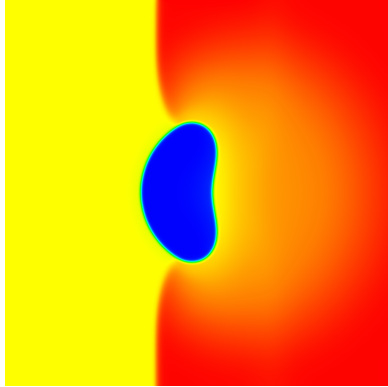


Figure 30.a:  $\rho$

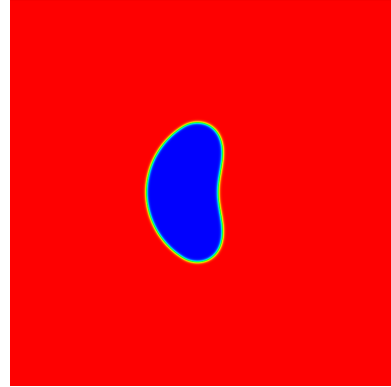


Figure 30.b:  $\phi$

Figure 30:  $\rho$  and  $\phi$  pseudocolor fields at  $t = 1.45 \cdot 10^{-4} \text{ s}$

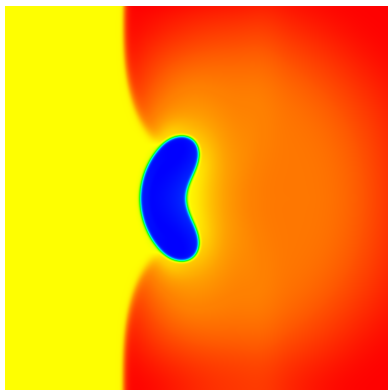


Figure 31.a:  $\rho$

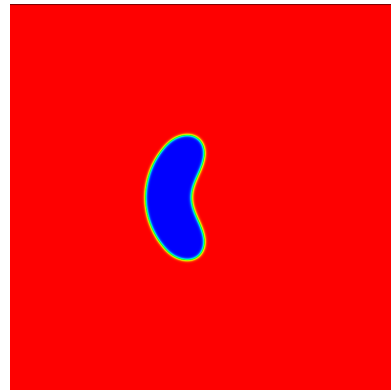


Figure 31.b:  $\phi$

Figure 31:  $\rho$  and  $\phi$  pseudocolor fields at  $t = 1.75 \cdot 10^{-4} \text{ s}$

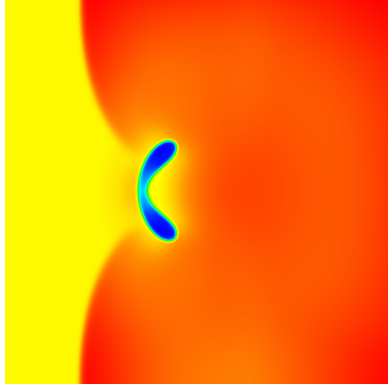


Figure 32.a:  $\rho$

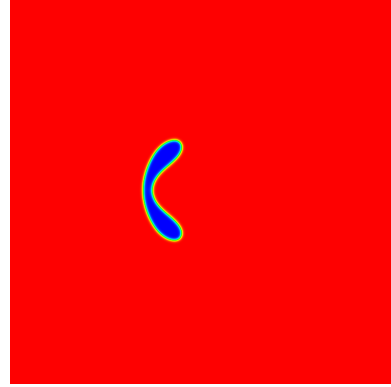


Figure 32.b:  $\phi$

Figure 32:  $\rho$  and  $\phi$  pseudocolor fields at  $t = 2.16 \cdot 10^{-4} \text{ s}$

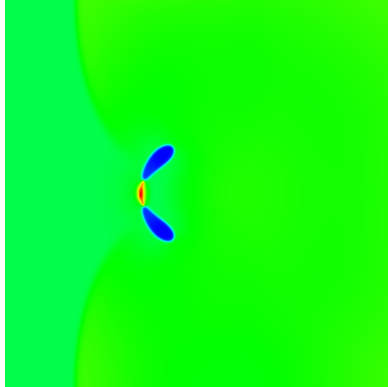


Figure 33.a:  $\rho$

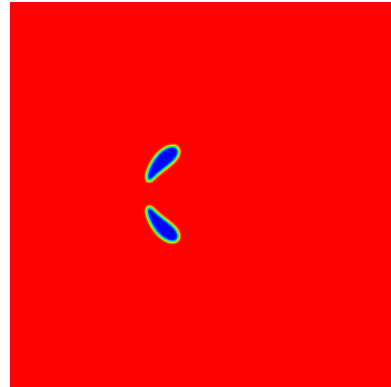


Figure 33.b:  $\phi$

Figure 33:  $\rho$  and  $\phi$  pseudocolor fields at  $t = 2.212 \cdot 10^{-4} \text{ s}$

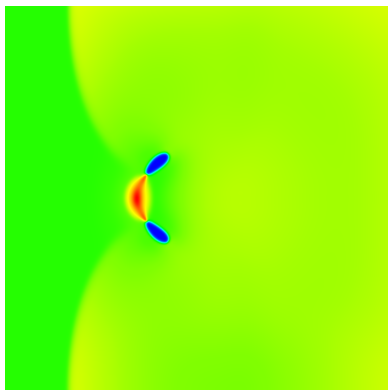


Figure 34.a:  $\rho$

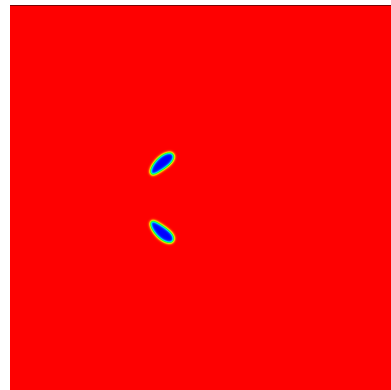


Figure 34.b:  $\phi$

Figure 34:  $\rho$  and  $\phi$  pseudocolor fields at  $t = 2.76 \cdot 10^{-4} \text{ s}$

## 7. Conclusion.

In this paper, an efficient numerical algorithm applicable to a wide range of compressible multicomponent flows has been built based on the linearized block implicit (LBI) factored schemes. Implicit nature of such schemes alongside low computational cost, due to the block-tridiagonal structure of the resulting system of linear algebraic equations, make them a powerful tool for solving flows at various Mach numbers, and for various values of viscosity. Although these schemes are known to produce a splitting error which is growing as the Mach number goes to zero, this error can be easily reduced, as has been demonstrated in this study.

Artificial dissipation term for high Mach number applications has been constructed as a finite difference interpretation of a novel finite element technique by Guermond and Popov from [4], which introduces artificial viscosity coefficients based on the maximum speed of propagation in local one dimensional Riemann problems. The estimation algorithm for the maximum speed of propagation proposed in [21] has been extended here to the case of stiffened gas equation of state. The Guermond-Popov method combines the robustness of classical first-order schemes, such as Lax-Friedrichs, while being less dissipative in space. No expensive Riemann solvers or flux limiters are needed for construction of the term.

A novel artificial dissipation term is proposed here for low Mach number applications. The term is based on second-order differences of conservative variables and product of conservative variables and corresponding Jacobians. Such a combination is shown to be able to fight the odd-even decoupling problem while controlling the total kinetic energy of the system. This allows the use of LBI factored scheme in terms of conservative variables on non-staggered grids for low Mach number applications.

The form of the dissipation terms allows one to couple the technique with interface-capturing approach without disrupting the interfacial equilibrium. It is achieved by introducing the proper function of EOS coefficients as variables. The sharpening technique from [25] is shown to be compatible with the method, and with a CSF implementation of the surface tension from [6].

Possible extensions and directions for further research may include a use of more accurate time-marching methods or a defect-correction technique to lift the order of accuracy of the algorithm, a development of a nonlinear adaptive procedure to define the scaling of LM-dissipation term (i.e. choice of  $\omega_1$  and  $\omega_2$ ), a more detailed study of the CSF surface tension model, including its conservative and non-conservative formulations, as well as alternative approximations for interfacial curvature and implicit treatment of the CSF-term, developing a version of the algorithm for staggered grids, incorporating implicit non-reflection boundary conditions, and extending the method to the three dimensional case and more complicated geometry.

## 8. Acknowledgements.

I wish to thank professor R. Krechetnikov for suggesting the original idea and problem formulation for the project, professor P. Mineev for his guidance and pieces of advice throughout this work, creators of VisIt (see [52]) and ParaView (see [53]) applications and LAPACK (see [54]) library for providing extremely helpful pieces of software.

## 9. Appendix A. Governing Equations and computation of Jacobians.

The governing equations (compressible Navier-Stokes and advection of SG EOS coefficients) can be written as

$$\begin{aligned} \frac{\partial U}{\partial t} + A \frac{\partial F(U)}{\partial x} + B \frac{\partial G(U)}{\partial y} &= \frac{\partial V_1(U, U_x)}{\partial x} + \frac{\partial V_2(U, U_y)}{\partial x} \\ &+ \frac{\partial W_1(U, U_x)}{\partial y} + \frac{\partial W_2(U, U_y)}{\partial y} + F^{ST} \end{aligned} \quad (124)$$

where

$$U = [\rho \quad m \quad n \quad E \quad \alpha \quad \beta]^T \quad (125)$$

$$F = \left[ m \quad \frac{m^2}{\rho} + p \quad \frac{mn}{\rho} \quad (E + p) \frac{m}{\rho} \quad \alpha \quad \beta \right]^T \quad (126)$$

$$G = \left[ n \quad \frac{nm}{\rho} \quad \frac{n^2}{\rho} + p \quad (E + p) \frac{n}{\rho} \quad \alpha \quad \beta \right]^T \quad (127)$$

$$F^{ST} = [0 \quad \sigma \kappa \partial_x \phi \quad \sigma \kappa \partial_y \phi \quad \sigma \kappa u \partial_x \phi + \sigma \kappa v \partial_y \phi \quad 0 \quad 0]^T \quad (128)$$

$$V_1 = \left[ 0 \quad \frac{4\mu}{3} \partial_x \frac{m}{\rho} \quad \mu \partial_x \frac{n}{\rho} \quad \frac{4\mu m}{3\rho} \partial_x \frac{m}{\rho} + \mu \frac{n}{\rho} \partial_x \frac{n}{\rho} \quad 0 \quad 0 \right]^T \quad (129)$$

$$V_2 = \left[ 0 \quad \frac{-2\mu}{3} \partial_y \frac{n}{\rho} \quad \mu \partial_y \frac{m}{\rho} \quad \frac{-2\mu m}{3\rho} \partial_y \frac{n}{\rho} + \mu \frac{n}{\rho} \partial_y \frac{m}{\rho} \quad 0 \quad 0 \right]^T \quad (130)$$

$$W_1 = \left[ 0 \quad \mu \partial_x \frac{n}{\rho} \quad -\frac{2\mu}{3} \partial_x \frac{m}{\rho} \quad \frac{-2\mu n}{3\rho} \partial_x \frac{m}{\rho} + \mu \frac{m}{\rho} \partial_x \frac{n}{\rho} \quad 0 \quad 0 \right]^T \quad (131)$$

$$W_2 = \left[ 0 \quad \mu \partial_y \frac{m}{\rho} \quad \frac{4\mu}{3} \partial_y \frac{n}{\rho} \quad \frac{\mu m}{3\rho} \partial_y \frac{m}{\rho} + \frac{4\mu n}{3\rho} \partial_y \frac{n}{\rho} \quad 0 \quad 0 \right]^T \quad (132)$$

where  $\mu$  [kg/(s · m)] is a dynamic viscosity coefficient,  $\sigma$  [N/m] is the surface tension coefficient,  $\phi$  is the volume of fluid function,  $\kappa = -\nabla \cdot \frac{\nabla \phi}{|\nabla \phi|}$  is the interfacial curvature.

$$A = \begin{bmatrix} 1 & 0 & 0 & 0 & 0 & 0 \\ 0 & 1 & 0 & 0 & 0 & 0 \\ 0 & 0 & 1 & 0 & 0 & 0 \\ 0 & 0 & 0 & 1 & 0 & 0 \\ 0 & 0 & 0 & 0 & \frac{m}{\rho} & 0 \\ 0 & 0 & 0 & 0 & 0 & \frac{m}{\rho} \end{bmatrix} \quad (133)$$

$$B = \begin{bmatrix} 1 & 0 & 0 & 0 & 0 & 0 \\ 0 & 1 & 0 & 0 & 0 & 0 \\ 0 & 0 & 1 & 0 & 0 & 0 \\ 0 & 0 & 0 & 1 & 0 & 0 \\ 0 & 0 & 0 & 0 & \frac{n}{\rho} & 0 \\ 0 & 0 & 0 & 0 & 0 & \frac{n}{\rho} \end{bmatrix} \quad (134)$$

$$p = \frac{1}{\alpha} \left( E - \frac{m^2 + n^2}{2\rho} - \beta \right). \quad (135)$$

After time discretization (124) becomes

$$\begin{aligned} \frac{U^{n+1} - U^n}{\tau} + A^n \frac{\partial F^{n+1}(U)}{\partial x} + B^n \frac{\partial G^{n+1}(U)}{\partial y} = \\ \frac{\partial V_1^{n+1}(U, U_x)}{\partial x} + \frac{\partial V_2^n(U, U_y)}{\partial x} + \frac{\partial W_1^n(U, U_x)}{\partial y} + \frac{\partial W_2^{n+1}(U, U_y)}{\partial y} \end{aligned} \quad (136)$$

which is linearized as

$$F^{n+1} = F^n + \left( \frac{\partial F}{\partial U} \right)^n (U^{n+1} - U^n) \quad (137)$$

$$G^{n+1} = G^n + \left( \frac{\partial G}{\partial U} \right)^n (U^{n+1} - U^n) \quad (138)$$

$$V_1^{n+1} = V_1^n + \left( \frac{\partial V_1}{\partial U} \right)^n (U^{n+1} - U^n) + \left( \frac{\partial V_1}{\partial U_x} \right)^n (U_x^{n+1} - U_x^n) \quad (139)$$

$$W_2^{n+1} = W_2^n + \left( \frac{\partial W_2}{\partial U} \right)^n (U^{n+1} - U^n) + \left( \frac{\partial W_2}{\partial U_y} \right)^n (U_y^{n+1} - U_y^n) \quad (140)$$

where

$$\frac{\partial F}{\partial U} = \begin{bmatrix} 0 & 1 & 0 & 0 & 0 & 0 \\ f_1 & \frac{2m}{\rho} - \frac{m}{\alpha\rho} & -\frac{n}{\alpha\rho} & \frac{1}{\alpha} & f_2 & -\frac{1}{\alpha} \\ -\frac{mn}{\rho^2} & \frac{n}{\rho} & \frac{m}{\rho} & 0 & 0 & 0 \\ f_3 & \frac{E+p}{\rho} - \frac{m^2}{\alpha\rho^2} & -\frac{mn}{\alpha\rho^2} & \frac{m}{\rho} \left(1 + \frac{1}{\alpha}\right) & f_4 & -\frac{m}{\alpha\rho} \\ 0 & 0 & 0 & 0 & 1 & 0 \\ 0 & 0 & 0 & 0 & 0 & 1 \end{bmatrix} \quad (141)$$

where  $f_1 = -\frac{m^2}{\rho^2} + \frac{1}{\alpha} \left( \frac{m^2+n^2}{2\rho^2} \right)$ ,  $f_2 = -\frac{1}{\alpha^2} \left( E - \frac{m^2+n^2}{2\rho} - \beta \right)$ ,  
 $f_3 = -\frac{(E+p)m}{\rho^2} + \frac{m^3+mn^2}{2\alpha\rho^3}$ ,  $f_4 = -\frac{m}{\alpha^2\rho} \left( E - \frac{m^2+n^2}{2\rho} - \beta \right)$ .

$$\frac{\partial G}{\partial U} = \begin{bmatrix} 0 & 0 & 1 & 0 & 0 & 0 \\ -\frac{mn}{\rho^2} & \frac{n}{\rho} & \frac{m}{\rho} & 0 & 0 & 0 \\ g_1 & -\frac{m}{\alpha\rho} & \frac{2n}{\rho} - \frac{n}{\alpha\rho} & \frac{1}{\alpha} & g_2 & -\frac{1}{\alpha} \\ g_3 & -\frac{mn}{\alpha\rho^2} & \frac{E+p}{\rho} - \frac{n^2}{\alpha\rho^2} & \frac{n}{\rho} \left(1 + \frac{1}{\alpha}\right) & g_4 & -\frac{n}{\alpha\rho} \\ 0 & 0 & 0 & 0 & 1 & 0 \\ 0 & 0 & 0 & 0 & 0 & 1 \end{bmatrix} \quad (142)$$

where  $g_1 = -\frac{n^2}{\rho^2} + \frac{1}{\alpha} \left( \frac{m^2+n^2}{2\rho^2} \right)$ ,  $g_2 = -\frac{1}{\alpha^2} \left( E - \frac{m^2+n^2}{2\rho} - \beta \right)$ ,



$$g_3 = -\frac{(E+p)n}{\rho^2} + \frac{n^3+nm^2}{2\alpha\rho^3}, \quad g_4 = -\frac{n}{\alpha^2\rho} \left( E - \frac{m^2+n^2}{2\rho} - \beta \right).$$

$$\frac{\partial V_1}{\partial U} = \begin{bmatrix} 0 & 0 & 0 & 0 & 0 & 0 \\ -\frac{4\mu}{3} \left( \frac{\partial_x m}{\rho^2} - \frac{2m\partial_x \rho}{\rho^3} \right) & -\frac{4\mu}{3} \frac{\partial_x \rho}{\rho^2} & 0 & 0 & 0 & 0 \\ -\mu \left( \frac{\partial_x n}{\rho^2} - \frac{2n\partial_x \rho}{\rho^3} \right) & 0 & -\mu \frac{\partial_x \rho}{\rho^2} & 0 & 0 & 0 \\ v_1 & v_2 & v_3 & 0 & 0 & 0 \\ 0 & 0 & 0 & 0 & 0 & 0 \\ 0 & 0 & 0 & 0 & 0 & 0 \end{bmatrix} \quad (143)$$

$$\text{where } v_1 = -\frac{4\mu}{3} \left( \frac{2m\partial_x m}{\rho^3} - \frac{3m^2\partial_x \rho}{\rho^4} \right) - \mu \left( \frac{2n\partial_x n}{\rho^3} - \frac{3n^2\partial_x \rho}{\rho^4} \right), \quad v_2 = \frac{4\mu}{3} \left( \frac{\partial_x m}{\rho^2} - \frac{2m\partial_x \rho}{\rho^3} \right), \quad v_3 = \mu \left( \frac{\partial_x n}{\rho^2} - \frac{2n\partial_x \rho}{\rho^3} \right).$$

$$\frac{\partial V_1}{\partial U_x} = \begin{bmatrix} 0 & 0 & 0 & 0 & 0 & 0 \\ -\frac{4\mu}{3} \frac{m}{\rho^2} & \frac{4\mu}{3\rho} & 0 & 0 & 0 & 0 \\ -\frac{\mu n}{\rho^2} & 0 & \frac{\mu}{\rho} & 0 & 0 & 0 \\ -\frac{4\mu}{3} \frac{m^2}{\rho^3} - \frac{\mu n^2}{\rho^3} & \frac{4\mu}{3} \frac{m}{\rho^2} & \frac{\mu n}{\rho^2} & 0 & 0 & 0 \\ 0 & 0 & 0 & 0 & 0 & 0 \\ 0 & 0 & 0 & 0 & 0 & 0 \end{bmatrix} \quad (144)$$

$$\frac{\partial W_2}{\partial U} = \begin{bmatrix} 0 & 0 & 0 & 0 & 0 & 0 \\ -\mu \left( \frac{\partial_y m}{\rho^2} - \frac{2m\partial_y \rho}{\rho^3} \right) & -\mu \frac{\partial_y \rho}{\rho^2} & 0 & 0 & 0 & 0 \\ -\frac{4\mu}{3} \left( \frac{\partial_y n}{\rho^2} - \frac{2n\partial_y \rho}{\rho^3} \right) & 0 & -\frac{4\mu}{3} \frac{\partial_y \rho}{\rho^2} & 0 & 0 & 0 \\ w_1 & w_2 & w_3 & 0 & 0 & 0 \\ 0 & 0 & 0 & 0 & 0 & 0 \\ 0 & 0 & 0 & 0 & 0 & 0 \end{bmatrix} \quad (145)$$

$$\text{where } w_1 = -\frac{4\mu}{3} \left( \frac{2n\partial_y n}{\rho^3} - \frac{3n^2\partial_y \rho}{\rho^4} \right) - \mu \left( \frac{2m\partial_y m}{\rho^3} - \frac{3m^2\partial_y \rho}{\rho^4} \right), \quad w_2 = \mu \left( \frac{\partial_y m}{\rho^2} - \frac{2m\partial_y \rho}{\rho^3} \right), \quad w_3 = \frac{4\mu}{3} \left( \frac{\partial_y n}{\rho^2} - \frac{2n\partial_y \rho}{\rho^3} \right).$$

$$\frac{\partial W_2}{\partial U_x} = \begin{bmatrix} 0 & 0 & 0 & 0 & 0 & 0 \\ -\mu \frac{m}{\rho^2} & \frac{\mu}{\rho} & 0 & 0 & 0 & 0 \\ -\frac{4\mu}{3} \frac{n}{\rho^2} & 0 & \frac{4\mu}{3} \frac{1}{\rho} & 0 & 0 & 0 \\ -\frac{4\mu}{3} \frac{n^2}{\rho^3} - \frac{\mu m^2}{\rho^3} & \mu \frac{m}{\rho^2} & \frac{4\mu}{3} \frac{n}{\rho^2} & 0 & 0 & 0 \\ 0 & 0 & 0 & 0 & 0 & 0 \\ 0 & 0 & 0 & 0 & 0 & 0 \end{bmatrix} \quad (146)$$

## References

## References

- [1] W. Briley, H. McDonald, On the structure and use of linearized block implicit schemes, Journal of Computational Physics 34 (1) (1980) 54–73.
- [2] R. Beam, R. Warming, An implicit factored scheme for the compressible Navier-Stokes equations, AIAA journal 16 (4) (1978) 393–402.

- [3] D. Choi, C. Merkle, Application of time-iterative schemes to incompressible flow, *AIAA Journal* 23 (10) (1985) 1518–1524.
- [4] J.-L. Guermond, B. Popov, Invariant domains and first-order continuous finite element approximation for hyperbolic systems, *SIAM Journal on Numerical Analysis* 54 (4) (2016) 2466–2489.
- [5] R. Saurel, R. Abgrall, A simple method for compressible multifluid flows, *SIAM Journal on Scientific Computing* 21 (3) (1999) 1115–1145.
- [6] G. Perigaud, R. Saurel, A compressible flow model with capillary effects, *Journal of Computational Physics* 209 (1) (2005) 139–178.
- [7] S. Klainerman, A. Majda, Singular limits of quasilinear hyperbolic systems with large parameters and the incompressible limit of compressible fluids, *Communications on Pure and Applied Mathematics* 34 (4) (1981) 481–524.
- [8] S. Klainerman, A. Majda, Compressible and incompressible fluids, *Communications on Pure and Applied Mathematics* 35 (5) (1982) 629–651.
- [9] H. Guillard, C. Viozat, On the behaviour of upwind schemes in the low Mach number limit, *Computers & Fluids* 28 (1) (1999) 63–86.
- [10] H. Guillard, A. Murrone, On the behavior of upwind schemes in the low Mach number limit: Ii. Godunov type schemes, *Computers & Fluids* 33 (4) (2004) 655–675.
- [11] E. Turkel, R. Radespiel, N. Kroll, Assessment of preconditioning methods for multidimensional aerodynamics, *Computers & Fluids* 26 (6) (1997) 613–634.
- [12] E. Turkel, Preconditioning techniques in computational fluid dynamics, *Annual Review of Fluid Mechanics* 31 (1) (1999) 385–416.
- [13] F. Cordier, P. Degond, A. Kumbaro, An asymptotic-preserving all-speed scheme for the Euler and Navier-Stokes equations, *Journal of Computational Physics* 231 (17) (2012) 5685–5704.
- [14] G. Dimarco, R. Loubère, M.-H. Vignal, Study of a new asymptotic preserving scheme for the Euler system in the low Mach number limit.
- [15] R. Klein, Semi-implicit extension of a Godunov-type scheme based on low Mach number asymptotics i: One-dimensional flow, *Journal of Computational Physics* 121 (2) (1995) 213–237.
- [16] H. Zakerzadeh, S. Noelle, A note on the stability of implicit-explicit flux splittings for stiff hyperbolic systems, *IGPM Preprint* (449) (2016) 2–1.
- [17] R. Beam, R. Warming, An implicit finite-difference algorithm for hyperbolic systems in conservation-law form, *Journal of Computational Physics* 22 (1) (1976) 87–110.
- [18] A. Samarskii, V. P.N., *Additivnie skhemi dlya zadach matematicheskoy fiziki* (in Russian), Moskva Nauka, 1999.
- [19] K.-B. Kong, J.-S. Kim, S.-O. Park, Reduced splitting error in the ADI-FDTD method using iterative method, *Microwave and Optical Technology Letters* 50 (8) (2008) 2200–2203.
- [20] V. Coralic, T. Colonius, Finite-volume WENO scheme for viscous compressible multicomponent flows, *Journal of Computational Physics* 274 (2014) 95–121.
- [21] J.-L. Guermond, B. Popov, Fast estimation from above of the maximum wave speed in the Riemann problem for the Euler equations, *Journal of Computational Physics* 321 (2016) 908–926.
- [22] F. Miczek, F. Röpke, P. Edelmann, New numerical solver for flows at various Mach numbers, *Astronomy & Astrophysics* 576 (2015) A50.
- [23] F. Miczek, Simulation of low Mach number astrophysical flows, Ph.D. thesis, Universität München (2013).
- [24] G. Allaire, S. Clerc, S. Kokh, A five-equation model for the simulation of interfaces between compressible fluids, *Journal of Computational Physics* 181 (2) (2002) 577–616.
- [25] R. Shukla, C. Pantano, J. Freund, An interface capturing method for the simulation of multi-phase compressible flows, *Journal of Computational Physics* 229 (19) (2010) 7411–7439.
- [26] R. Abgrall, How to prevent pressure oscillations in multicomponent flow calculations: a quasi conservative approach, *Journal of Computational Physics* 125 (1) (1996) 150–160.
- [27] R. Abgrall, S. Karni, Computations of compressible multifluids, *Journal of Computational Physics* 169 (2) (2001) 594–623.
- [28] X.-D. Liu, R. Fedkiw, S. Osher, A conservative approach to the multiphase Euler equations without spurious pressure oscillations.
- [29] A. Chertock, S. Karni, A. Kurganov, Interface tracking method for compressible multifluids, *ESAIM: Mathematical Modelling and Numerical Analysis* 42 (6) (2008) 991–1019.
- [30] S. Shin, D. Juric, Modeling three-dimensional multiphase flow using a level contour reconstruction method for front tracking without connectivity, *Journal of Computational Physics* 180 (2) (2002) 427–470.
- [31] T. Liu, B. Khoo, K. Yeo, Ghost fluid method for strong shock impacting on material interface,

- Journal of Computational Physics 190 (2) (2003) 651–681.
- [32] T. Hou, P. LeFloch, Why nonconservative schemes converge to wrong solutions: error analysis, *Mathematics of Computation* 62 (206) (1994) 497–530.
  - [33] S. Karni, Multicomponent flow calculations by a consistent primitive algorithm, *Journal of Computational Physics* 112 (1) (1994) 31–43.
  - [34] C. A. Fletcher, *Computational techniques for fluid dynamics*. Volume 1-Fundamental and general techniques. Volume 2-Specific techniques for different flow categories, in: Berlin and New York, Springer-Verlag, 1988, p. Vol. 1, 418 p.; vol. 2, 493 p., Vol. 1, 1988.
  - [35] J.-L. Guermond, P. Mineev, A new class of massively parallel direction splitting for the incompressible Navier-Stokes equations, *Computer Methods in Applied Mechanics and Engineering* 200 (23) (2011) 2083–2093.
  - [36] W. Briley, H. McDonald, Reflections on the evolution of implicit Navier-Stokes algorithms, *Computers & Fluids* 41 (1) (2011) 15–19.
  - [37] V. Ryaben’kii, S. Tsynkov, *A theoretical introduction to numerical analysis*, CRC Press, 2006.
  - [38] H. Francis, A. Anthony, Technical report LA-4700, Tech. rep. (1971).
  - [39] D. Jacqmin, An energy approach to the continuum surface tension method, *AIAA paper* (96-0858).
  - [40] D. Jamet, D. Torres, J. Brackbill, On the theory and computation of surface tension: the elimination of parasitic currents through energy conservation in the second-gradient method, *Journal of Computational Physics* 182 (1) (2002) 262–276.
  - [41] M. Francois, S. Cummins, E. Dendy, D. Kothe, J. Sicilian, M. Williams, A balanced-force algorithm for continuous and sharp interfacial surface tension models within a volume tracking framework, *Journal of Computational Physics* 213 (1) (2006) 141–173.
  - [42] E. Toro, *Riemann solvers and numerical methods for fluid dynamics: a practical introduction*, Springer Science & Business Media, 2013.
  - [43] K. Haller, Y. Ventikos, D. Poulikakos, Wave structure in the contact line region during high speed droplet impact on a surface: Solution of the Riemann problem for the stiffened gas equation of state, *Journal of Applied Physics* 93 (5) (2003) 3090–3097.
  - [44] S. R. Chakravarthy, Euler equations-Implicit schemes and boundary conditions, *AIAA Journal*(ISSN 0001-1452) 21 (1983) 699–706.
  - [45] G. Sod, A survey of several finite difference methods for systems of nonlinear hyperbolic conservation laws, *Journal of Computational Physics* 27 (1) (1978) 1–31.
  - [46] G. Taylor, A. Green, Mechanism of the production of small eddies from large ones, *Proceedings of the Royal Society of London. Series A, Mathematical and Physical Sciences* 158 (895) (1937) 499–521.
  - [47] A. J. Chorin, Numerical solution of the Navier-Stokes equations, *Mathematics of Computation* 22 (104) (1968) 745–762.
  - [48] W. Barsukow, P. V. Edelmann, C. Klingenberg, F. Miczek, F. Röpke, A numerical scheme for the compressible low-Mach number regime of ideal fluid dynamics, *Journal of Scientific Computing* 72 (2) (2017) 623–646.
  - [49] E. Johnsen, T. Colonius, Numerical simulations of non-spherical bubble collapse, *Journal of Fluid Mechanics* 629 (2009) 231–262.
  - [50] R. Nourgaliev, S. Y. Sushchikh, T.-N. Dinh, T. Theofanous, Shock wave refraction patterns at interfaces, *International Journal of Multiphase Flow* 31 (9) (2005) 969–995.
  - [51] K. Thompson, Time dependent boundary conditions for hyperbolic systems, *Journal of Computational Physics* 68 (1) (1987) 1–24.
  - [52] H. Childs, E. Brugger, B. Whitlock, J. Meredith, S. Ahern, D. Pugmire, K. Biagas, M. Miller, C. Harrison, G. Weber, H. Krishnan, T. Fogal, A. Sanderson, C. Garth, E. Bethel, D. Camp, O. Rübel, M. Durant, J. Favre, P. Navrátil, VisIt: An End-User Tool For Visualizing and Analyzing Very Large Data, in: *High Performance Visualization—Enabling Extreme-Scale Scientific Insight*, 2012, pp. 357–372.
  - [53] J. Ahrens, B. Geveci, C. Law, *Paraview: An end-user tool for large data visualization*, *The Visualization Handbook* 717.
  - [54] E. Anderson, Z. Bai, C. Bischof, S. Blackford, J. Demmel, J. Dongarra, J. Du Croz, A. Greenbaum, S. Hammarling, A. McKenney, D. Sorensen, *LAPACK Users’ Guide*, 3rd Edition, Society for Industrial and Applied Mathematics, Philadelphia, PA, 1999.